NTNU
Innovation and Creativity

Velocity Estimation in muscular Tissue by Ultrasound

Trond-Olav Dahl

Master of Science in Communication Technology
Submission date: June 2007
Supervisor: Tor Audun Ramstad, IET
Co-supervisor: Hans Torp, ISB

Norwegian University of Science and Technology
Department of Electronics and Telecommunications

Problem Description

The modified autocorrelation method (MAM) has shown to be superior to the conventional autocorrelation method (AM) in simulation environments. However, this superiority is not present in results from in vivo experiments. In order to understand these inconsistent results the simulation model will be extended to include acoustic and thermal noise, and aliasing. The influence of clutter filtering and aliasing correction on MAM and AM is then to be investigated.

Clutter will be added to the model as a low-pass process, while aliasing can be achieved by decimation in the time domain. Existing methods for clutter filtering and aliasing correction will be implemented and tested. New methods can be developed and tested if found necessary. The chosen methods will be applied to in-vivo data of the septum and compared to simulations.

Assignment given: 15. January 2007
Supervisor: Tor Audun Ramstad, IET

Abstract

When estimating tissue velocities, the conventional autocorrelation method (AM) is only biased if the demodulation frequency is correctly estimated. While AM assumes the received centre frequency to be constant, the modified autocorrelation method (MAM) estimates the received centre frequency continuously from pulse to pulse. Although MAM has shown superior performance in simulation environments, it fails to show consistently better performance compared to AM when applied to experimental data. In order to investigate this lack of consistency, a model for simulation of signal from moving tissue was developed, including realistic aspects such as thermal noise, signal from clutter and aliasing. The simulation model was adapted using experimental tissue data and parameters from a true acquisition system. A 1st order FIR filter was applied for clutter rejection prior to velocity estimation.

The investigations using simulation data shown faster performance degradation of MAM compared to AM when the amount of signal from clutter or thermal noise were increased independently. For clutter signal mimicking acoustic noise from reverberations, MAM went from significantly better under low-noise conditions to approaching AM performance when the signal-to-clutter ratio became lower than 10 dB. Analogously, MAM approached AM performance when the signal-to-noise ratio was lower than 15 dB.

Velocity estimation of experimental data shown MAM's robustness to frequency dependent attenuation by means of frequency compensation, while AM suffered from bias effects due to erroneously estimated demodulation frequency. The frequency compensation did, however, not succeed to approve lower estimation variance in MAM compared to AM. Statistical analysis based on expected values from simulations, demonstrated correlation between the estimation error in AM and MAM.

Preface

This thesis fulfills the requirements for a degree of Master at the Norwegian University of Science and Technology (NTNU). My formal supervisor has been professor Tor A. Ramstad at the Department of Electronics and Telecommunications. The work was however carried out at the Department of Circulation and Medical Imaging, NTNU, and has been based on previously unpublished work by the writer. Daily supervision was given by professor Hans Torp and PhD Student Svein Arne Aase.

Acknowledgements

First of all, I would like thank Hans Torp for outlining the problem to be assessed in this work. Further, I would like to thank Svein Arne Aase for his help and patience in the lab. I would like to thank them both for their encourage and the interest they have shown in my work, which has been a great inspiration for me. Also, I would like to thank my student colleagues at the Department of Circulation and Medical Imaging for social as well as academic contributions. Finally, thanks to Tor A. Ramstad for being listed as my supervisor.

Jessheim, June 19, 2007

Trond-Olav Dahl

Contents

1 Introduction **1**

2 Background **3**
2.1 Diagnostic ultrasound imaging 3
2.1.1 Background 3
2.1.2 Principles of ultrasound imaging 4
2.1.3 Building blocks of an ultrasound imaging system . . . 7
2.1.4 Image quality 9
2.1.5 Ultrasound Doppler imaging 10
2.2 Tissue Doppler Imaging 13
2.2.1 Background 13
2.2.2 Data acquisition 14
2.2.3 Signal model 16
2.2.4 Clutter signal separation 18
2.2.5 Tissue velocity estimation 19

3 Methods and implementation **23**
3.1 Tools 23
3.1.1 MATLAB 23
3.1.2 GCMat 23
3.1.3 Ultrasound equipment and setup 23
3.2 The simulation model 24
3.2.1 Acquisition system 24
3.2.2 Signal from moving tissue 25
3.2.3 Signal from clutter 27
3.2.4 Signal loss and thermal noise 28
3.2.5 Statistic Gaussian signal 29
3.2.6 Aliasing 29
3.3 Simulation model verification 32
3.4 Simulation model set-up 32
3.4.1 Pulse centre frequency and bandwidth 32
3.4.2 Pulse beam width 33
3.4.3 Temporal signal length 33

3.4.4 Parameter set-up . . . 34
3.5 Using the simulation model . . . 34
3.5.1 Signal-to-noise ratio . . . 35
3.5.2 Signal-to-clutter ratio . . . 35
3.5.3 Aliasing . . . 36
3.5.4 Angle dependency . . . 36
3.5.5 Pulse bandwidth . . . 36
3.6 Experimental data acquisition . . . 37
3.7 Tissue velocity estimation . . . 38
3.7.1 Clutter filtering . . . 38
3.7.2 Autocorrelation methods . . . 39
3.7.3 Cross-correlation method . . . 39

4 Results **43**
4.1 Simulation model verification . . . 43
4.1.1 Frequency analysis . . . 43
4.1.2 RF-domain analysis . . . 43
4.2 Simulation model set-up . . . 48
4.2.1 Pulse centre frequency and bandwidth . . . 48
4.2.2 Temporal signal length . . . 48
4.3 Clutter filtering . . . 49
4.4 Velocity estimation on simulation data . . . 52
4.4.1 Presence of thermal noise . . . 52
4.4.2 Presence of clutter . . . 52
4.4.3 Aliasing . . . 52
4.4.4 Angle dependency . . . 56
4.4.5 Pulse bandwidth . . . 56
4.5 Velocity estimation on experimental data . . . 59

5 Discussion **63**
5.1 Simulation model verification . . . 63
5.2 Simulation model set-up . . . 64
5.3 Clutter filtering . . . 65
5.4 Velocity estimation on simulation data . . . 65
5.5 Velocity estimation on experimental data . . . 67

6 Conclusion **69**
Bibliography . . . 71

List of Figures

2.1 Reflection principle in wave propagation 5
2.2 Beam profiles for unfocused and focused transducers 6
2.3 Block diagram of a typical ultrasound system. The figure is found in [8]. 7
2.4 The Doppler effect 10
2.5 Illustration of signal acquisition in TDI. 15
2.6 Investigation of amplitude distribution in myocardial tissue. . 18

3.1 Simulated transducer pulse 25
3.2 Simulated signal from moving tissue 26
3.3 Gaussian shaped clutter signal in Doppler frequency 27
3.4 Simulated clutter signal in the 2D power spectrum 28
3.5 Simulated signal from thermal noise in the 2D power spectrum 29
3.6 Received simulation signal made statistic Gaussian. 30
3.7 Decimation of simulation signal in IQ-domain 31
3.8 B-mode image of the left ventricle in a healthy human heart . 33
3.9 1. order FIR filter for clutter rejection 38
3.10 Cross-correlation estimation using sub-segment 40

4.1 Spectrum of simulated pulse versus received simulated signal 44
4.2 Simulated RF-signal with different SNR 45
4.3 Simulated RF-signal with different SCR 46
4.4 Simulated RF-signal with aliasing and not 47
4.5 Estimated spectra of experimental versus simulation data . . 48
4.6 Estimated standard deviation as a function of temporal samples 49
4.7 Clutter filter effects in the 2D power spectrum 50
4.8 Velocity estimation statistics as a function of FIR attenuation 51
4.9 Velocity estimation statistics as a function of SNR 53
4.10 Velocity estimation statistics as a function of SCR 54
4.11 Velocity estimation statistics as function of axial velocity . . 55
4.12 Velocity estimation statistics as a function of intersection angle 57
4.13 Velocity estimation statistics as a function of pulse bandwidth 58
4.14 Septum of a human heart applied to velocity estimation . . . 59
4.15 Estimated radial frequency content in experimental data . . . 60

4.16 Velocity curves, biased AM 61
4.17 Velocity curves and estimation difference, compensated AM . 62

List of Tables

3.1 Experimental parameter set-up. 24
3.2 Simulation model parameter set-up 35

4.1 Values for standard deviation from Figure 4.11. 55

Chapter 1

Introduction

Since the early 90's, Tissue Doppler Imaging (TDI) has been developed as a clinical tool to quantify regional myocardial function. In 1998, Heimdal et. al [4] introduced a velocity-based method for regional deformation imaging, referred to as Strain Rate Imaging. One-dimensional strain rate measures the speed of local deformation along the beam direction as the difference in axial velocity between two points a known distance apart. Due to this gradient operation, strain rate has shown to be very sensitive to noise [11], and its performance, therefore, heavily depends on the velocity estimator used. Most known methods for velocity estimation are based on the autocorrelation function, and today the conventional autocorrelation method is widely used. Another such method, referred to as the modified autocorrelation method (MAM), was introduced in by Loupas et al. [12] in order to improve velocity estimates. While the conventional autocorrelation method assumes the center frequency of the received ultrasound signal to be constant from pulse to pulse, MAM estimates the received center frequency continuously.

Although MAM in previous work has shown superior results when applied to simulated data [3, 12], the results are contradictory in experimental data. Applied to blood velocity estimation in [7] resulted in a reduced estimator bias and variance. On the contrary, estimation bias and variance were lower for AM than MAM, when applied to strain rate estimation on experimental data in [3].

The purpose of this work is to investigate possible causes the modified autocorrelation method not consistently shows better performance than the conventional method in-vivo experiments. A comparison of the two methods will be made together with the cross-correlation method (CCM) in a controlled environment. First, this involves development of a simulation model for received signal in Tissue Doppler Imaging. By including essential aspects present in real ultrasound acquisition, the simulation model intends to clarify the inconsistency in results when MAM is applied to data from simulations and experiments. In this work, the most important aspects are

considered to be acoustic and thermal noise, and aliasing. Second, spectral analysis on data acquired with GE Vingmed Ultrasound's Vivid 7 will be carried out and used as reference in setting up the simulation model. This to make the simulation model more realistic in terms of tissue velocity estimation purposes. Next, the velocity estimators, implemented in previous work not published, will be applied to data from the simulation model. The different aspects will be investigated separately to assess their influence in tissue velocity estimation, and then to point out one or more candidates that to a greater extent introduce estimation errors to the modified autocorrelation method than the conventional one. Finally, the velocity estimators will be applied to data from the septum of a healthy human heart for comparison based on results from simulations. The correlation between estimation error in AM and MAM will be investigated by means of statistical analysis.

This thesis is organized as follows: An introduction to basic principles in ultrasound imaging is given in Chapter 2, including a description of Tissue Doppler Imaging. Chapter 3 includes the methods of this work, while the results are presented in Chapter 4. Next, Chapter 5 contains discussion of the presented results based on knowledge attained in Chapter 2. Finally, Chapter 6 states the conclusion of the work.

Chapter 2

Background

The following section aims to give the unfamiliar reader a brief introduction to principles, terms and methods related to diagnostic ultrasound. This chapter also contains more detailed description of the modality under investigation in this thesis work, the concept of Tissue Doppler Imaging (TDI).

2.1 Diagnostic ultrasound imaging

2.1.1 Background

Diagnostic ultrasound had its humble start in the early 1940's, when two Austrian brothers managed to generate an image using ultrasonic waves in an attempt to locate a brain tumor [11]. The concept of using ultrasonic waves to image the human interior was based on knowledge from pulse-echo SONAR and technology from metal flaw detectors available at the time. As a result of research into its diagnostic use in the late 40's, the first descriptions of diagnostic ultrasound was reported in the early 50's in the United States by Wild & Reid and Howry & Bliss, and in Europe by Edler & Hertz [5]. The discovery of new piezoelectric material during the 40's, that allowed for short pulses in the MHz range, was a necessity for the technology to be used in medicine.

The pioneer groups demonstrated in the early 50's that ultrasound as a diagnostic tool was able to detect tissue layers, tumors and heart structures. A decade later the first commercial instruments to offer static images of the human interior became available. In such instruments, B-mode scanners (brightness mode), the image is based on amplitudes, more precisely the envelope of the amplitudes, in the received echo. Improved transistor technology during the 60's made real-time B-mode imaging feasible on commercial scanners by the end of the decade.

Some years earlier, in 1957 Satumora proposed an continuous wave (CW) ultrasound system to detect movements based on the Doppler shift of the received signal. The lack of depth information in CW systems lead to a

pulsed wave (PW) approach in the late 60's, which was able to measure blood flow in a vessel at an explicit depth. In the mid-eighties, the modality was combined with B-mode imaging, allowing the Doppler signal to be superimposed on the B-mode image in real-time [5, 8].

Ultrasound imaging has a number of advantages over other imaging systems. There are no building requirements as for X-ray and MR, the equipment is relatively cheap and transportable, and its real-time capabilities can give rapid diagnosis while being being safe and painless to the patient [1, 5]. Today ultrasound imaging is probably best known for applications during pregnancy and obstetric. Cardiovascular diagnosis utilize the high frame rate imaging in qualitative analysis of the heart muscle deformation and blood flow in the heart and arteries, while Doppler imaging provide quantitative measurements on tissue velocities and blood flow. Other areas in medicine where ultrasound imaging has found its application is in detection of cancer and as a tool for quality control in the operating theatre.

The following section gives a brief description on the principles in ultrasound imaging.

2.1.2 Principles of ultrasound imaging

Ultrasound are acoustic waves with frequencies higher than 20 kHz, making them undetectable for the human ear. Diagnostic ultrasound make use of acoustic waves with centre frequencies in the range of $2 - 15$ MHz. When an acoustic wave travels through some medium the particles will oscillate around their equilibrium position along the wave's direction, making it a longitudinal wave. Therefore, no net displacement takes place and no mass is transported – it is only the wave that travels. As an ultrasound wave propagate in human tissue it interacts with medium having different acoustic properties, which result in the back-scattered signal that makes ultrasound imaging possible. An image can then be formed, based on the amplitudes in the received signal.

Density ρ and adiabatic compressibility κ are the two factors describing the acoustic properties of a homogeneous medium. By assumption of energy conservation, the acoustic pressure waves in a homogeneous medium is completely described by (2.1) for linear propagation, which means the particle displacement is linearly proportional to the instantaneous pressure [2].

$$\nabla^2 p(\mathbf{r}, t) - \frac{1}{c^2} \frac{\partial p(\mathbf{r}, t)}{\partial t^2} = 0 \tag{2.1}$$

Here $\mathbf{r}$ is the spatial position vector, t is time and $c = \sqrt{\frac{1}{\rho\kappa}}$ is the speed of sound in a medium characterized by ρ and κ. In water sound travels with a speed of 1480 m/s, and in human tissue, which consists of mostly water, the speed has been measured to be 1540 m/s on average [8]. In medical

ultrasound the assumption of constant propagation speed is an important convention to achieve a simple, unambiguous relation to depth in pulsed wave echo.

In conventional ultrasound a pressure pulse is transmitted into the tissue by a transducer as illustrated in Figure 2.1. When the propagating wave encounters a boundary between two different tissue structures, one part of the wave is reflected while the other continues its propagation. The amount of reflection depends on the two media's difference in acoustic properties, while the other wave possibly continues its propagation in a new direction (not illustrated in the figure), dependent on the speed of sound in the two media [5].

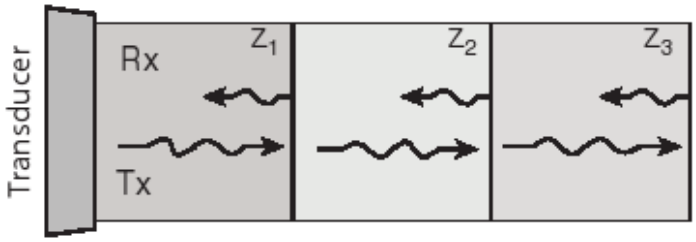

Figure 2.1: Illustration of the essential reflection principle in wave propagation. When a propagating wave encounters a boundary between two different media, the wave is partly reflected. The figure is found in [8]

Clear boundaries rarely exist in the human body. A propagating wave is more likely to encounter areas with varying acoustic properties, which constitutes a set of reflecting objects. The type of reflection from such objects depends entirely on their size compared to the wavelength. Objects larger than the wavelength reflects the wave in a specular way, while objects of comparable size to the wavelength reflects the wave directionally. When the object is smaller than the wavelength, it scatters the signal in an omni-directional way, so-called Rayleigh-scattering. The total signal from many scatterers result in a destructive and constructive interference pattern that give the image a grainy appearance, referred to as speckle. Due to scattering, the back-scattered signal can be characterized in statistical terms. The amplitude distribution in back-scattered signal from human tissue is statistic Gaussian with zero mean and some variance, dependent on the deviation in acoustic properties of the penetrated medium [5].

The ultrasonic wave is attenuated as it propagates through some medium. Two main factors to attenuation is absorption and scattering. Absorption is conversion into thermal energy and amounts to $75-95$ % [5] of the total energy loss. This attenuation limits the penetration depth in ultrasound imaging. Increasing frequency of the transmitted pulse results in higher image resolution, but, since the attenuation is frequency dependent the penetration

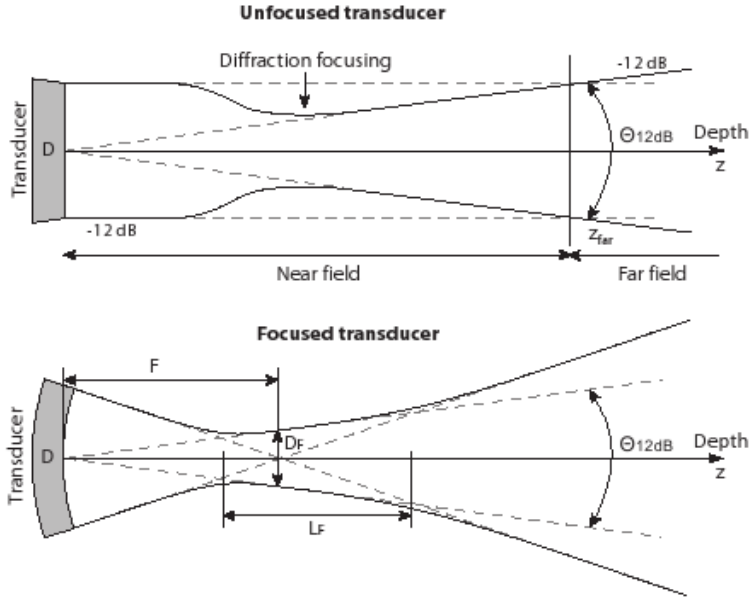

Figure 2.2: Beam profiles for unfocused and focused transducers, in upper and lower plot, respectively. The unfocused beam suffers from diffraction effects in the near field, which cause convergence of the beam known as diffraction focusing. A narrow beam width is achieved over a limited depth by means of focusing. The figure is found in [8].

depth is reduced. Therefore the choice of pulse frequency is a compromise between image resolution and penetration depth [1]. Another consequence of the frequency dependent attenuation is the change in spectrum of the received pulse, as the higher frequency components are attenuated to a greater extent than the lower. The attenuation in human tissue is approximately 0.5 dB/[MHz cm] one way [1].

Beam formation

The upper plot in Figure 2.2 illustrates a directional sound beam. The beam becomes directional as a consequence of a small wavelength of the transmitted pressure wave compared to the transmitting aperture. That is, the directionality increases when the transmitted frequency increases. It is convenient to divide the beam course into near and far field. The extreme near field is often defined as the region where the beam width is approximately the same as the aperture used. On the other hand, the far field is defined as the region where the pressure wave amplitude fall of at a fixed rate. Diffraction effects in the near field cause the beam to converge, a phenomenon called diffraction focusing. For a plane circular transducer, the transition between the near and far field is given by

$$z_{far} = \frac{D^2}{2\lambda}, \tag{2.2}$$

where D is the diameter of the aperture, and λ is the wavelength of the transmitted pulse. In medical ultrasound, image formation is made in the near field of the transducer.

A focused beam can be achieved at a specific depth in a limited region by curving the aperture, by using a lens, or by using transducer arrays and electronic delays between the different array elements. In order to achieve efficient focusing, the focus point must lie within the near field, as shown in the lower plot of Figure 2.2. For a focused transducer, the beam width D_F defines the lateral resolution of the imaging system, given by (-3 dB beam width)

$$D_F = \frac{\lambda}{D}F = F_{\#}\lambda, \tag{2.3}$$

where F is the distance to the focus point, D is the aperture diameter, and λ is the emitted wavelength. $F_{\#}$, the F-number of the imaging system, is the focus distance measured in apertures. Moreover, the effective depth region of uniform beam width as given at the focus depth is denoted focal depth, given by (-1 dB beam width)

$$L_F = 4 \cdot \lambda F_{\#}^2. \tag{2.4}$$

In order to achieve narrow beam width in focus, the $F_{\#}$ is desired to be low. However, as the focal depth depends on the $F_{\#}$ squared, using too low F-number can concentrate the sound energy in small region along the beam axis. As a consequence, the F-number must be optimized with respect to transducer and application. [8]

2.1.3 Building blocks of an ultrasound imaging system

This section deals with the composition of imaging systems used in diagnostic ultrasound. Typical building blocks and signal chain for such systems are shown in Figure 2.3, and will be described in the following.

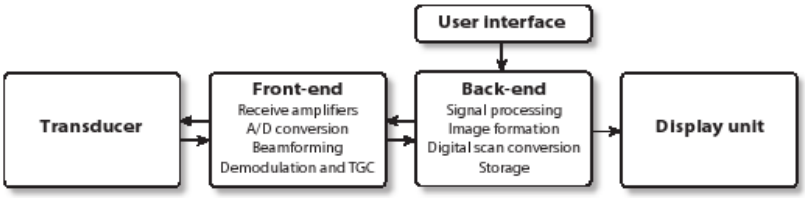

Figure 2.3: Block diagram of a typical ultrasound system. The figure is found in [8].

Transducer

The transducer is responsible for transmission and reception of ultrasonic pressure waves, typically consisting of an array of piezoelectric elements. On transmission, an external electric field cause vibrations in the piezoelectric material that results in ultrasonic waves. Analogously, on reception, the elements vibrate as a consequence of external pressure, creating an electrical signal. The size and shape of the transducer must be chosen with respect to clinical application. Further, as a given application demands certain penetration depth, the piezoelectric material is designed to work in a specific frequency range. As an example, a transducer designed for cardiac imaging must be small enough to fit between the ribs, with typical working frequency in the range from 2-4 MHz in order to achieve sufficient penetration. [8]

Front-end

The front-end consist of hardware responsible for controlling the transmission and reception of ultrasonic waves by the transducer. In order to direct the beam in one direction, the necessary delays are calculated in the front-end. In receive mode, a delay-and-sum procedure realises beam-forming of the received signal from the transducer elements into one direction. A filter matched to the bandwidth of the received signal is applied in order to maximize the signal-to-noise ratio. Furthermore, as the attenuation is depth dependent, echoes from deeper structures are amplified in order to be images simultaneously with structures placed close to the transducer. This concept is called time-gain compensation. Finally, the RF-signal is brought to baseband through complex demodulation in order to reduce the number of samples, thus, the demand for storage for later processing. [8]

Back-end

The back-end of an ultrasound system is responsible for a number of tasks involving user interfacing, signal processing, image preparation and scan conversion, and archive storage of ultrasound recordings. In modern systems, these tasks are performed in software on a real-time aware operating system on a conventional desktop computer. Typically, the back-end computer first processes user interface tasks before communicating with and setting up the front-end for new operations. A number of tasks have been moved from front-end to the back-end due to development in computer technology, which give more flexible and cost effective systems than earlier hardware solutions could offer. Example of such tasks are image filtering, Doppler processing and scan conversion. [8]

2.1.4 Image quality

Spatial resolution

The spatial resolution is defined as the minimum spacing between two objects the imaging system is able to distinguish. In ultrasound imaging, the spatial resolution is theoretically determined by the centre frequency and bandwidth of the transmitted pulse, the aperture diameter, and the focus depth. The theoretical radial resolution is related to the temporal length of the emitted pulse T_{pulse} as

$$\Delta r = \frac{c \cdot T_{pulse}}{2} = \frac{c}{2 \cdot B_{pulse}}, \tag{2.5}$$

where B_{pulse} is the pulse bandwidth. In other words, the radial resolution is first of all limited by the transducer bandwidth. Furthermore, it is degraded by frequency dependent attenuation, which shift the frequency content of the received pulse towards zero. As the lateral resolution is defined by the beam width, given by Eq. (2.3), it depends on the F-number and wavelength of the emitted pulse. [8]

Factors corrupting image quality

The image quality in ultrasound systems is reduced by different factors related to physical phenomenons and to system design. A brief description of factors related to this work is given below.

Reverberations: Conventional ultrasound imaging assumes only one scattering process before reception at the transducer. However, the ultrasound wave may encounter multiple reflections on its way. This phenomenon, referred to as reverberations, result in ghost images as a consequence of several receptions of signal from specific scatterers.

Frequency dependent attenuation: Frequency dependent attenuation shifts the frequency content towards zero during wave propagation. The reduced centre frequency results in lower spatial resolution and penetration. The effect increases with depth.

Beam side-lobes: Beam side-lobes are present due to the finite transducer aperture. A scatterer in a side-lobe will therefore be registered on receive, reducing the contrast resolution of the image.

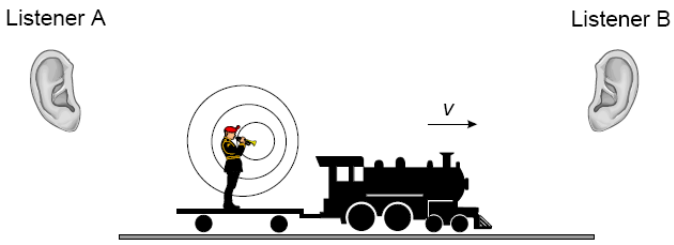

Figure 2.4: The two listeners observe different frequency if the sound source is moving like indicated. The figure is found in [5].

2.1.5 Ultrasound Doppler imaging

If an acoustic source is moving relative to the observer, the observed frequency is different from the frequency transmitted by the source. This phenomenon is termed after Christian Doppler, who first proposed the effect in 1842 in an attempt to explain the colour of the stars. The observed frequency f_R will be given by [5]

$$f_R = \frac{c + v_o}{c - v_s} f_T, \tag{2.6}$$

where f_T is the transmitted frequency,v_o is the speed of the observer, v_s is the speed of the source and c is the speed of sound. The velocity is defined as positive when the motion is towards the other.

Figure 2.4 shows two stationary listeners observing a continuous tone from a source moving relatively to each of them. Due to the trumpet's motion towards listener B, the listener experiences a frequency f_{R_B} that is higher than the frequency f_T transmitted by the trumpet. The observed frequency f_{R_B} for listener B is then given by

$$f_{R_B} = \frac{c}{c - v_s} f_T, \tag{2.7}$$

where v_s is the trumpet's velocity towards listener B.

When an ultrasound wave interacts with objects moving relatively to the source, the reflected wave will experience a slight shift in frequency. The Doppler effect contradicts or expands the timescale of waves reflected from moving scatterers or emitted by moving sources. Both of these cases occur in conventional ultrasound. The scaling of the temporal axis can be expressed as [5]:

$$\alpha = \frac{c + v\cos\theta}{c - v\cos\theta} \approx (1 + \frac{2v\cos\theta}{c}), \tag{2.8}$$

where θ is the angle between the scatterer velocity and the ultrasound beam, $v\cos\theta$ is the axial velocity component of the scatterer, defined positive to-

wards the transducer. The corresponding Doppler shift is then given by

$$f_d = \alpha f_0 - f_0 = 2f_0 \frac{v \cos\theta}{c}, \tag{2.9}$$

where the Doppler shift is termed f_d and f_0 is the emitted frequency. The equation is valid as long as $v \cos\theta \ll c$.

The Doppler principle can be utilized to measure velocities of flowing blood or moving tissue by ultrasound. Normal velocity of blood flow can reach up to 1 m/s, while stenotic and valve defection can cause blood flows up to 6 m/s. The highest tissue velocities is found in the heart, where the myocardium contractions can be in the range up to 10 cm/s, while the movement of heart valves can have velocities up to 50 cm/s.

The backscattered signal from tissue is a sum of contributions from several scatterers, each producing their own Doppler shift, resulting in a spectra of different velocities in the received signal. Moreover, due to the fact that each scatterer is observed in a finite time interval, a non-zero bandwidth is given for each single velocity contribution. This effect is referred to as the transit time effect.

Spectral analysis of the received signal can provide velocity information of a given sample volume. As the Doppler shifted signal is in the audible range, it is common to make the signal audible through a set of speakers for interpretation. For blood velocities, listening to the output gives an impression of the blood flow. This modality was the only modality available in the first Doppler instruments before real-time spectral analysis became feasible. Two different pulse excitation approaches have become standard in Doppler imaging, one based on continuous wave and a second based on pulsed waves. A brief description will now be given. [8]

Continuous-wave Doppler

In continuous-wave Doppler (CW-Doppler), a single frequency sinusoidal is continuously transmitted into the tissue, while the echo signal is simultaneously picked up, typically by another part of the transducer. Because the sample volume is determined by the overlap between the transmit and receive beam, range resolution is in practice not available in CW-Doppler. Due to its continuous nature, the main advantage of CW-Doppler is that it is not limited in maximum velocity.

The magnitude and sign of the Doppler frequency can be obtained by quadrature demodulation. Consider the emission given by [8]

$$e(t) = \cos(2\pi f_0 t) = Re\{e^{i2\pi f_0 t}\}, \tag{2.10}$$

where f_0 is the emitted sinusoidal frequency. The received signal at time t after emission, assumed to be a delayed, scaled and Doppler shifted version

of the emitted signal at time t_0, is then given by:

$$r(t) = A(\alpha(t-t_0)) \cdot e(\alpha(t-t_0)) = A(\alpha(t-t_0)) \cdot \cos(2\pi f_0 \alpha(t-t_0)) \quad (2.11)$$

The complex analytic signal received is obtained through the Hilbert transform, and given by:

$$\tilde{r}(t) = \widetilde{A}(\alpha(t-t_0)) \cdot e^{2\pi\alpha f_o(t-t_0)} \quad (2.12)$$

Mixing the analytic received signal with the quadrature reference signal $e^{-i2\pi f_o t}$ reveals the Doppler signal:

$$\begin{aligned} r_{IQ} &= \widetilde{A}(\alpha(t-t_0)) \cdot e^{i2\pi\alpha f_0(t-t_0)} \cdot e^{-i2\pi f_0 t} \\ &= \widetilde{A}(\alpha(t-t_0)) \cdot e^{i2\pi(\alpha f_0 - f_0)t - i2\pi\alpha f_0 t_0} \\ &= \widetilde{A}(\alpha(t-t_0)) \cdot e^{i2\pi f_d t + i\phi_0} \end{aligned} \quad (2.13)$$

Pulsed-wave Doppler

In Pulsed-wave Doppler (PW-Doppler), series of pulses are emitted into the tissue at a constant pulse repetition frequency (PRF). Range resolution is obtained by sampling the received echo at a fixed time after transmission, using pulse length shorter than the time between two pulse emissions $T_{PRF} = \frac{1}{PRF}$. As the pulses interact with moving scatterers, they are shifted in frequency according to (2.9). However, the change in bandwidth due to frequency dependent attenuation can be large compared to the Doppler shift itself, making it difficult to measure the Doppler shift as in CW-Doppler. Instead, another approach to measure the velocity of scatterers is taken, based on the difference between two pulses received subsequently. The signal from consecutive emissions will be delayed an amount proportional to the axial velocity of the scatterers. For a simple illustration of this, pulse interaction with a single scatterer is considered. The emitted pulse typically consist of a burst of sinusoidal oscillations, as given in complex form by

$$e(t) = g(t)e^{i2\pi f_0 t}, \quad (2.14)$$

where $g(t)$ is the complex envelope of the pulse and f_0 is the pulse carrier frequency. Considering a single scatterer at depth r_0, moving with velocity v and angle θ compared to the beam and pulses emitted at the rate $\frac{1}{T_{PRF}}$, the received signal from a pulse emitted at time t can then be described by

$$r_m(t) = e(\alpha(t-t_m)), \quad (2.15)$$

where α is the time compression factor given in (2.8), and t_m is the relative time from pulse emission to reception for pulse number m, given by

$$t_m = \frac{2r_o}{c} + \frac{2v\cos\theta m T_P}{c} = t_0 + m\tau. \tag{2.16}$$

The relation between two consecutive received pulses then becomes

$$r_m(t) = e(\alpha(t-t_0)) = e(\alpha(t - t_0 - \frac{2v\cos\theta m T_P}{c})) = r_{m-1}(t-\tau), \tag{2.17}$$

which in this ideal case is a delayed version of the previous pulse. The parameter τ, which contain the velocity information, can be estimated, either directly from consecutive RF-signals, or by sampling the resulting change in phase compared to the carrier frequency between consecutive pulses. Conventional PW-Doppler ultrasound make use of the latter procedure. Inserting (2.14) into the expression for $r_m(t)$ gives

$$r_m(t) = g(\alpha(t-t_0))e^{i2\pi f_0\alpha(t-t_0-m\tau)} = g(\alpha(t-t_m))e^{i2\pi f_0\alpha(t-t_0)}e^{i\phi(m)}, \tag{2.18}$$

where the phase function is given by

$$\phi(m) = 2\pi f_0 \alpha \frac{2v\cos\theta T_P}{c} m. \tag{2.19}$$

The instantaneous frequency of this phase function, estimated by discrete derivative, then becomes

$$f_\phi = \frac{1}{2\pi}\frac{\phi(m)-\phi(m-1)}{T_P} = 2f_o\alpha\frac{v\cos\theta}{c} \approx f_d. \tag{2.20}$$

This equation is valid for $v\cos\theta \ll c$. As seen, the instantaneous Doppler-shift is actually an artefact in PW-Doppler systems. In conventional PW-Doppler systems, this signal, referred to as the complex Doppler signal, is obtained by removing the carrier frequency through complex demodulation. The sign of the Doppler signal can be found by investigating the phase relationship between the in phase and quadrature components. [8]

2.2 Tissue Doppler Imaging

2.2.1 Background

Tissue Doppler Imaging (TDI) is a modality for combined quantification and visualization of tissue movements, first reported by McDicken et al. in 1992 [9]. In this modality, the velocity estimates are colour coded superimposed on a B-mode image for clinicians to assess myocardial regional function. As tissue movements are mainly situated in the heart, the clinical community often refer to it as Colour Doppler Myocardial Imaging. Furthermore, local deformation of the heart is an interesting measure for clinicians, and a velocity-based approach was described by Heimdal et al. in 1998 [4].

One-dimensional strain rate measures the speed of deformation along the ultrasound beam, based on two axial velocity estimates a known distance apart. Unfortunately, the method is demonstrated very sensitive to noise in the velocity estimates [11].

Estimation of the complete Doppler spectrum for each range gate is not a practical solution for TDI. Consequently, effort was put into research for a suitable estimator with respect to the few samples available for processing. In the mid-eighties, Kasai and Namekawa introduced an autocorrelation approach feasible for real-time systems, initially for estimation of blood flow [6]. Today, the autocorrelation estimator is the standard algorithm in most modern commercial scanners for velocity estimation of blood and tissue.

The basic signal processing blocks in TDI includes data acquisition, clutter signal separation, tissue velocity estimation, and tissue velocity visualisation. In short, after data acquisition, N_P samples are available for processing for each sample bin in the image. Prior to velocity estimation, the signal is processed to remove the clutter signal due to reverberations or side-lobe effects. After velocity estimation, the velocities are conventionally encoded in different colours and visualised superimposed on a gray-scaled B-mode image. A more detailed description of data acquisition, clutter signal separation and velocity estimation in TDI will now be given.

2.2.2 Data acquisition

The data acquisition in TDI is based on pulsed wave excitation. As the ultrasonic beam is scanned over the region to be imaged, N_P pulses are transmitted and received in each direction. This acquisition scheme is referred to as packet acquisition and N_P is the packet-size. There are some challenges in TDI acquisition. A sufficiently high spatial resolution, needed to investigate local changes in the two-dimensional velocity, is obtained using high-bandwidth pulses. However, the signal-to-noise ratio decrease with bandwidth and longer pulses must often be used to achieve adequate sensitivity. This compromises the spatial resolution, and also requires a separate acquisition of B-mode images.

Frame rate represents another challenge in TDI acquisition. A high packet-size is desired to efficiently separate the signal of moving tissue from clutter. On the other hand, a high frame rate is required to follow the dynamics of the tissue motion. In TDI, the packet-size is therefore limited by the frame rate, often to the minimum at 3. A higher frame rate can be achieved by reducing the sampling of lateral beams, however, this will reduce the lateral resolution and the image quality, and again a compromise is made. Modern scanners often offer multi-line acquisition (MLA). In this acquisition scheme, several receive beams are generated on each beam transmission, and the frame rate is increased at the expense of more beam-forming hardware [8].

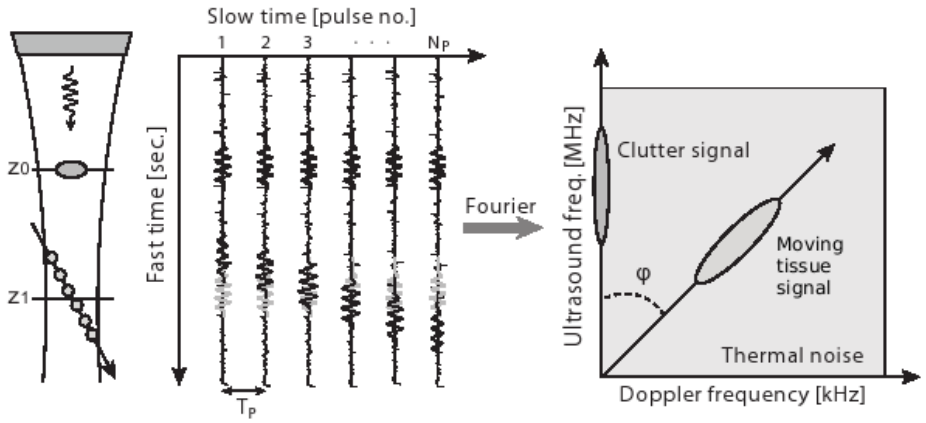

Figure 2.5: Illustration of signal acquisition in TDI. Signal from a strong reflector at depth z_0, representing clutter, and a moving scatterer at depth z_1, representing moving tissue, is acquired by subsequent pulse emissions. The acquired signal along the beam is termed the fast-time signal, while the signal from subsequent emissions at a specific depth is termed the slow-time signal. The corresponding frequency content in Fourier domain is shown to the right. The figure is adapted from [8]

The received signal from each beam is sampled along depth range at a high rate ($\sim$ 50 MHz) and the obtained signal is referred to as the fast-time signal. Correspondingly, the signal obtained at a fixed depth from subsequently beam acquisitions is referred to as the slow-time signal. These concepts are shown in Figure 2.5, which illustrate the received signal from a stationary strong scatterer at depth z_0 and a moving scatterer at depth z_1 in presence of thermal noise. Combined, the fast-time and slow-time signal from a given range gate is available for velocity estimation in TDI. From corresponding frequency content, shown to the right, the signal from moving tissue can be seen spread out in both frequency dimensions, where the angle ϕ corresponds to the velocity of the moving scatterer.

The rate of subsequent pulse transmissions, the pulse repetition frequency (PRF), determines the sampling of the slow-time signal. The variation of the slow-time signal, given by the velocity of the scatterer, must therefore be lower than PRF/2, the Nyquist limit, in order to be correctly represented. If making use of only the slow-time signal in velocity estimation, the PRF is proportional to the maximum measurable velocity before aliasing occurs, while PRF is limited by the maximum depth to be imaged in order to avoid ambiguities as to where the signal is obtained from. In TDI this is avoided by waiting a suitable time before a new pulse is fired. By decreasing the PRF with a factor of k, there is time to obtain data in $k-1$ other directions, before transmitting the next pulse in the initial direction.

This technique is termed beam interleaving [8]. The number of beams k is called the interleave group size (IGS) and together they form an interleave group (IG). The interleave group size (IGS) can be expressed by

$$\text{IGS} = \left\lfloor \frac{\text{PRF}_{\max}}{\text{PRF}} \right\rfloor \cdot \text{MLA}, \tag{2.21}$$

where MLA is the number of beams received in parallel, and $\lfloor \cdot \rfloor$ means rounding off to nearest integer towards $-\infty$. Beam interleaving aims to maximize the overall frame rate given a user chosen PRF, according to the range of velocities in interest. [8]

2.2.3 Signal model

After acquisition the data sampled along slow-time and fast-time are organized in a two-dimensional matrix, as illustrated in Figure 2.5. The signal model in this work, based on N_P slow-time samples received at each range gate, and N_R fast-time samples in reach range bin, is then given by the complex matrix $\boldsymbol{x}$ as

$$\boldsymbol{x} = \begin{bmatrix} x_{1,1} & x_{1,2} & \dots & x_{1,N_P} \\ x_{2,1} & x_{2,2} & \dots & x_{2,N_P} \\ \vdots & \vdots & \ddots & \vdots \\ x_{N_R,1} & x_{N_R,2} & \dots & x_{N_R,N_P} \end{bmatrix} \tag{2.22}$$

In this general signal model, the received signal from an insonified sample volume is assumed to consist of three signal components. A moving tissue signal component $\boldsymbol{t}$ originating from sound scattered by tissue moving in the region of interest, a clutter signal component $\boldsymbol{c}$ originating from sound scattered by moving tissue in a region out of interest, due to acoustic noise sources as reverberations and beam side-lobes, and an electrical/thermal noise component $\boldsymbol{n}$. The general signal model is then given by

$$\boldsymbol{x} = \boldsymbol{t} + \boldsymbol{c} + \boldsymbol{n}. \tag{2.23}$$

Since the signal from moving tissue and clutter originate from scattering sources at different spatial locations, the two components are considered to be statistically independent. The thermal noise component is consider to have a large bandwidth compared to the sampling frequency PRF after receiver filtering, and therefore modeled as white noise.

When assuming the received signal from moving tissue and clutter to be a zero-mean complex Gaussian process, the probability density function (PDF) of the received matrix will be given by

$$p_x = \frac{1}{\pi^N |\boldsymbol{R}_x|} e^{-\boldsymbol{x}^{*T} \boldsymbol{R}_x^{-1} \boldsymbol{x}}. \tag{2.24}$$

The Gaussian signal is then uniquely described statistically by its second order moments, which is contained in the signal correlation matrix

$$\boldsymbol{R}_x = \mathrm{E}\{\boldsymbol{x}\boldsymbol{x}^{*T}\}, \tag{2.25}$$

where E denotes the expectation operator. Dealing with statistical independent signal component, this can be written as

$$\boldsymbol{R}_x = \boldsymbol{R}_t + \boldsymbol{R}_c + \boldsymbol{R}_n = \boldsymbol{R}_t + \boldsymbol{R}_c + \sigma_n^2 \boldsymbol{I}, \tag{2.26}$$

where $\boldsymbol{R}_t$ and $\boldsymbol{R}_c$ is the correlation matrix of moving tissue and clutter, respectively, σ_n^2 is the thermal noise variance, and $\boldsymbol{I}$ is the identity matrix. Stationarity is assumed in this framework.

A justification for assuming signal from moving tissue and clutter to be a zero-mean complex Gaussian process, will now be given.

Tissue signal model

Both clutter and moving tissue are assumed to originate from tissue in the signal model presented. Since tissue consist of scatterers of varying size compared to the wavelength of the ultrasound pulse, different scatter characteristics are present in the backscattered signal. The scattering properties can also vary with the angle of insonification. Tissue characterization based on analysis of backscattered pressure waves is still considered experimental. It is however well known that the received signal from randomly distributed scatterers is statistically Gaussian. This is assumed to be the case when modeling tissue in this work. When considering larger regions of non-uniform signal from tissue, a non-Gaussian distribution is typically observed due to big differences in reflections. It can however be justified, that when considering smaller regions of tissue with close to uniform distribution, the distribution of the received signal approaches a Gaussian shape. This phenomenon is illustrated in Figure 2.6, where the myocardial wall of a pig is imaged using an i13L linear array probe (GE Healthcare, WI, USA) operating at 14 MHz. The distribution of the tissue signal is observed to approach a Gaussian shape when smaller regions in the image is considered.

The Doppler signal received from tissue depends on the direction and velocity relative to the ultrasound probe of all scatterers in the group present within a resolution cell. Each scatterer contribute to the received Doppler signal with a Doppler shift, and a limited bandwidth due to the finite observation time related to the movement through the sample volume. Muscle contractions and muscle vibrations in the operator holding the ultrasound probe and patient are typical tissue movements that result in a Doppler shift. Because muscle contractions often are cyclic, and therefore are accelerated, they increase the bandwidth of the tissue Doppler spectrum. The transition between stationary fat and muscles that can result in reverberations, will

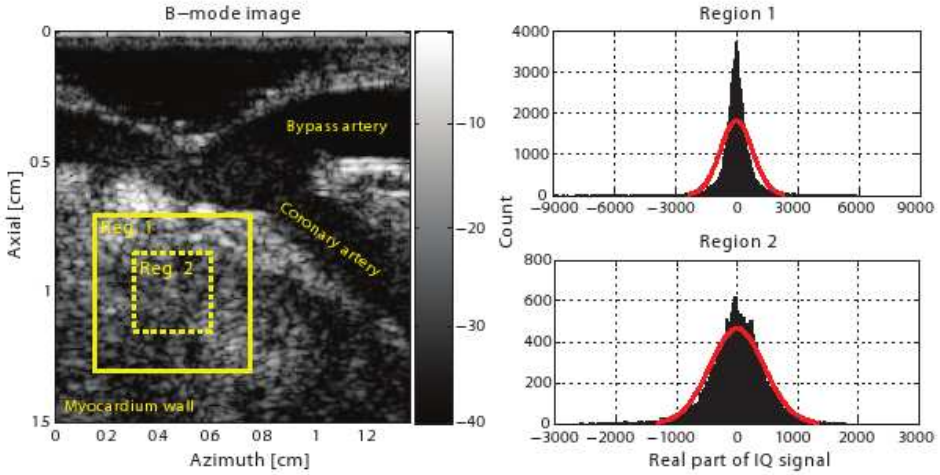

Figure 2.6: Investigation of amplitude distribution in signal from the myocardial wall of a pig. The distribution evidently approach Gaussian when the observed area becomes more uniform, as it will for smaller regions. The figure is found in [8].

therefore give a low Doppler-shift with some bandwidth according to the accelerated motion. [8]

2.2.4 Clutter signal separation

Due to beam side-lobes and reverberations, signal from surrounding structures may be present in the region of interest for velocity estimation. If the signal from these structures is not sufficiently attenuated it will introduce a significant bias to the velocity estimates. In conventional TDI, the clutter signal is removed by filtering in the slow-time domain. Besides sufficient attenuation in stop-band, the clutter filter is desired to have a short transition region in order to maintain the Doppler signal from moving tissue. A number of different approaches has been proposed for clutter filtering when a small number of temporal samples are available. The proposed approaches comprise finite impulse response (FIR), infinite impulse response (IIR) high-pass filters, and also polynomial regression filters [13]. In this work, the FIR filter approach is considered.

FIR filters can be described by an impulse response function $h(n)$ defined for $n = 0, \ldots, M-1$, where $M-1$ is denoted the filter order. The output signal $y(n)$ is then related to the input signal $x(n)$ through convolution, given by

$$y(n) = \sum_{k=0}^{M-1} h(k)x(n-k), \tag{2.27}$$

where the first $M-1$ output samples are invalid and discarded, thus, reducing the number of samples for velocity estimation. However, the advantages of FIR filters are low computational demands, easy implementation and the fact that they are time invariant.

2.2.5 Tissue velocity estimation

Velocity estimation in TDI utilize the change in RF or baseband signal received from moving scatterers. This change is observed over a few pulse emissions. Due to the limited number of temporal samples available, estimation of the full spectrum as in PW-Doppler, would result in poor spectrum estimates. Implementation wise, estimation of spectral parameters can be done in the frequency or time-domain. However, estimation in frequency domain is not a practical solution, due to the computational demands. Time-domain estimators obtain spectral information directly from samples, or by means of correlation analysis, and can have low computational demands.

The estimators are characterized by the signal information employed, as the slow-time signal only, or both the fast-time and slow-time signal can be exploited. Further the estimators are classified as narrowband or wideband estimators, in principle being valid for single frequency signal or general wide-band pulse emissions, respectively.

Phase-shift estimators utilize the fact that displacement of a scatterer between pulse emissions can be related to a change in shift in phase of the received signal compared to the demodulation frequency. The slow time signal only, or both the slow-time and fast-time signal can be employed by phase-shift estimators. Phase-shift techniques are computationally low demanding, and can also be done efficiently on baseband signals. However, phase-shift estimators are limited by aliasing, as the maximum phase-shift corresponding to a scatter displacement is $\pm\pi$.

Time-shift estimators are based on estimation of the time-delay of the received echoes due to a scatterer's displacement along the beam direction. Time-shift estimation techniques utilize both slow-time and fast-time signal in tracking the scatterer movement in the received RF-signal, and can in general offer estimates with lower bias and variance than estimation techniques that only employ the slow-time signal, also above the aliasing limit. However, time-shift estimators in general demand significant more computational power compared to phase-shift estimators, and the complexity is further increased when working on RF-signals.

The following section gives a brief description on the velocity estimators involved in this thesis work.

The autocorrelation estimator

The autocorrelation estimator was introduced by Kasai and Namekawa [6] in the mid-eighties, when real-time two-dimensional ultrasound velocity estimation first was shown feasible. The estimator was earlier described in the context of weather radar, where it was known as the correlated pulse-pair estimator. The autocorrelation approach utilizes the slow-time correlation function $R_x(n)$ at lag one in order to estimate the mean Doppler frequency, and the relation between the correlation function at lag one and the inverse Fourier transform of the Doppler spectrum $G(\omega)$ is, by means of the Wiener-Kinchin theorem, given by

$$R_x(1) = \frac{1}{2\pi}\int_{-\pi}^{\pi} G(\omega)e^{i\omega}d\omega = \frac{e^{i\bar{\omega}_d}}{2\pi}\int_{-\pi}^{\pi} G(\omega)e^{i(\omega-\bar{\omega}_d)}d\omega. \tag{2.28}$$

The mean Doppler frequency $\bar{\omega}_d$ can thus be estimated from the phase angle of $R_x(1)$ if the imaginary part of the last integral in Eq. (2.28) is zero. This criterion is fulfilled when dealing with spectra that are symmetric around its mean frequency, whereas a good approximation can be derived from narrowband spectra. [8]

The correlation function of lag one $\hat{R}_x(1)$, estimated from the received signal sequence, is related to the mean axial velocity of tissue $\hat{v}_z$ as

$$\hat{v}_z = \frac{c \cdot \mathrm{PRF}}{4\pi f_{dem}}\angle\hat{R}_x(1), \tag{2.29}$$

where f_{dem} is the demodulation frequency. The autocorrelation estimator is an unbiased estimator, also in presence of white noise, when the demodulation frequency corresponds to the true radial centre frequency of the received signal.

Any frequency dependent attenuation and random fluctuations in the radial centre frequency respectively introduce bias and variance in the autocorrelation estimator. To compensate for any variation in centre frequency, Loupas et al. introduced a two-dimensional autocorrelation approach in the mid-nineties [12] that estimates the received radial centre frequency $\hat{f}_0$ before velocity estimation. Explicit estimation of the radial centre frequency $\hat{f}_0$ can reduce the variance, by compensating for the random fluctuations, which cause similar fluctuations in the Doppler frequency, and to overcome the bias effect frequency dependent attenuation has on the autocorrelation estimator. The estimator makes use of the two-dimensional correlation function $R_x(m,n)$, where m and n denote samples in fast-time and slow-time, respectively. The fast-time correlation of lag one $\hat{R}_x(1,0)$, estimated from depth samples within a range bin, is related to the mean received radial frequency $\hat{f}_0$ as

$$\hat{f}_0 = f_{dem} + \frac{\angle \hat{R}_x(1,0)}{2\pi} f_{rs}, \tag{2.30}$$

where f_{rs} is the sampling frequency along depth. The mean axial velocity of tissue is further obtained by

$$\hat{v}_z = \frac{c \cdot \text{PRF}}{4\pi \hat{f}_0} \angle \hat{R}_x(0,1). \tag{2.31}$$

The estimator has shown to reduce the variance of the velocity estimates in simulated environments [12]. This result was supported in recent work in [3], where the estimator, here referred to as the modified autocorrelation method (MAM), outperformed the conventional autocorrelation method when estimating strain rate in a simulated environment. However, the same work found the conventional method to have a lower variance than the modified method when applied to strain rate estimation on experimental data. The modified autocorrelation estimator is, thus, still considered experimental.

The cross-correlation estimator

The cross-correlation estimator represents the time-shift estimators and is applied in the RF-domain. The concept of cross-correlation estimation is intuitively based as it tries to estimate the delay in the received signal. The delay τ, introduced in subsequent received pulses due to scatterer movement, was in Section 2.1.5 shown to be given by

$$\tau = \frac{2\Delta z}{c} = \frac{2v \cos\theta T_P}{c}. \tag{2.32}$$

The time delay can be estimated from the maximum correlation between two consecutive pulses r_1 and r_2 in a range segment, given by

$$\hat{\tau}_{max} = \arg\max R_{12}, \tag{2.33}$$

where the cross-correlation estimate for an explicit range segment in the RF-signal is given by [5]

$$\hat{R}_{12}(l') = \frac{1}{N_S} \sum_{k=0}^{N_S-1} r_1(k) r_2(k+l'), \tag{2.34}$$

where N_S is the number of range samples in a given range segment. Knowing the pulse emission interval T_P the axial velocity estimate is obtained from

$$\hat{v}_z = \frac{c}{2} \frac{\tau_{max}}{T_P}. \tag{2.35}$$

In contrast to the autocorrelation approach, where the estimated velocity is related to the mean velocity is the insonified region, the maximum lag

estimated by the cross-correlation approach is related to the velocity of the dominant scatterer in the region.

The cross-correlation technique, validated both in-vivo and in-vitro, can achieve lower variance estimate of the axial velocity compared to the conventional autocorrelation estimator, and is in theory not limited by aliasing. However, the increased performance compared to the autocorrelation approach is reduced when longer pulses must be used to obtain sufficient sensitivity. [8]

Chapter 3

Methods and implementation

This chapter describes the procedure of this work, comprising development, verification and adaption of a simulation model, acquisition of experimental data and implementation of velocity estimators. First, a brief description of the tools used for this purpose is given below.

3.1 Tools

3.1.1 MATLAB

In this work, all implementations and simulations are done in MATLAB version 7.2 R2006a installed on an IBM Thinkpad X41 having 1.5 GHz Intel Pentium M processor and 1.5 GB DDR2 RAM.

3.1.2 GCMat

GCMat is a tool for working with ultrasound data in MATLAB made by GE Vingmed in collaboration with Department of Circulation and Medical Imaging (ISB) at NTNU in Trondheim, Norway. The tool is able to import into MATLAB data stored in dicom format, which is the format GE Vingmed's scanners make use of, and through GCMat's graphical interface, the data can be presented in a sequence as they would appear on a scanner. To realise this GCMat utilizes only a part of its data processing functionality that also includes spectral analysis, conversion from IQ- to RF-data, among several others. In this work GCMat version 0.93b is used.

3.1.3 Ultrasound equipment and setup

Experimental data will be acquired with a modern high-end ultrasound scanner, the GE Vivid 7 ultrasound system, using a linear phased array transducer, the M3S. Essential set-up of acquisition parameters used in this work are listed in Table 3.1.

Parameter	Value
Center frequency, f_c	2.5 MHz
Demodulation frequency, f_{demod}	2.41 MHz
Pulse repetition frequency (PRF)	1 kHz
Pulse length	3 periods
Packet size	3
MLA	1
Aperture, D	2.2 cm
Radial IQ-samples	188

Table 3.1: Experimental parameter set-up.

3.2 The simulation model

This section describes the development of the simulation model to simulate acquired signal from moving tissue using ultrasound. For simplicity, only constant tissue velocity will be possible simulated by the model. The model will include acoustic and thermal noise, which is present in real ultrasound acquisition, as well as aliasing, which occur when the scatterers move faster, relative to the transducer, than the Nyquist velocity. In the following the implementation of the extended simulation model is described in detail and covers the acquisition system, simulation of signal from moving and stationary or slowly moving tissue, and thermal noise, and also simulation of aliasing in the received signal.

3.2.1 Acquisition system

In a pulsed-wave system, the transducer sends out a pulse before listening for the echo signal, which is statistical Gaussian from human tissue. The acquisition system does pre-processing on the signals before the data are visualised or used in estimation. For the simulation model, a one-beamed transducer and a receive filter constitute the simulated acquisition system, but the simulated transducer will only listen for echo, and the signal is not statistic Gaussian at the time of reception, but will be after reception. The transducer pulse is Gaussian shaped with some frequency f_0 and bandwidth B. Furthermore, the beam width will be determined in Section 3.4.2, based on experimental set-up parameters found in Table 3.1. While receive filters in true acquisition systems intend to maximize the received signal-to-noise ratio [13], its purpose in the simulation model is to limit the received signal in order to parametrise signal-to-noise and signal-to-clutter ratios, where the term *signal* here means signal only from moving tissue. The filter is realised by means of a Tukey-window with a bandwidth equal to -20 dB of

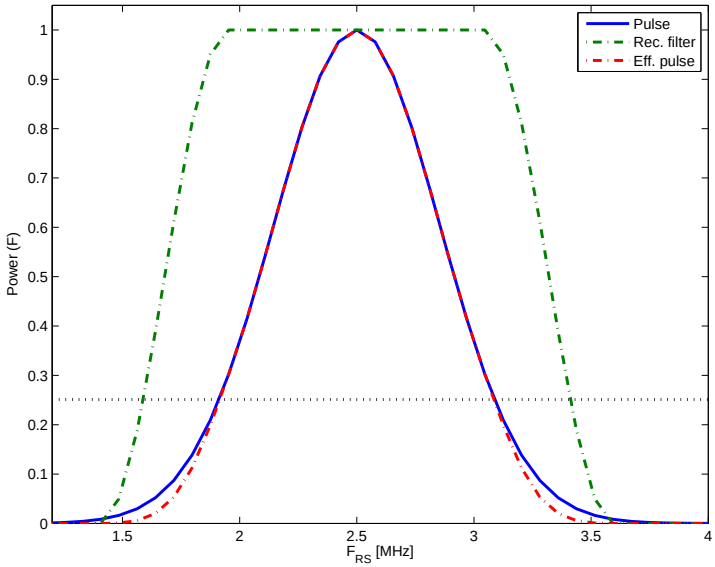

Figure 3.1: Simulated transducer pulse, receive filter and the effective pulse in power frequency domain.

pulse-peak value, B_{-20dB}. Figure 3.1 shows the simulated transducer pulse, the receive filter and the effective pulse after filtering. Here f_0 is 2.5 MHz and B_{-6dB} is 1.1 MHz, where the dotted line represents -6 dB of pulse-peak value. These two parameters are not fixed, but will be used in the following to describe the simulation model.

3.2.2 Signal from moving tissue

As was seen in Section , the signal spectrum from scatterers moving with constant velocity is concentrated along a straight line, with a slope proportional to the axial velocity. This line has some bandwidth inversely proportional to the time the scatterers are inside the sample volume, referred to as transit time. Since transit time depends on lateral velocity and beam width, the model includes intersection angle, which is set to 20° in order to approach a realistic environment.

From an implementation point of view, the starting point is a straight line in the 2D power spectrum representing scattered signal from moving tissue. Such a line is shown in Figure 3.2(a) for scatterers with axial velocity 5 cm/s and intersecting the beam in a 20° angle. Figure 3.2(c) shows the signal acquired with a by the simulated transducer when listening at the bandwidth defined by the pulse in Figure 3.1.

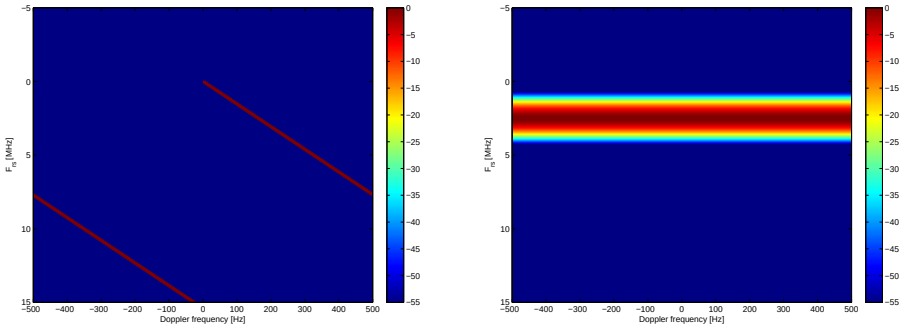

(a) Simulation of tissue moving with axial velocity 5 cm/s.

(b) Region covered by the ultrasound pulse

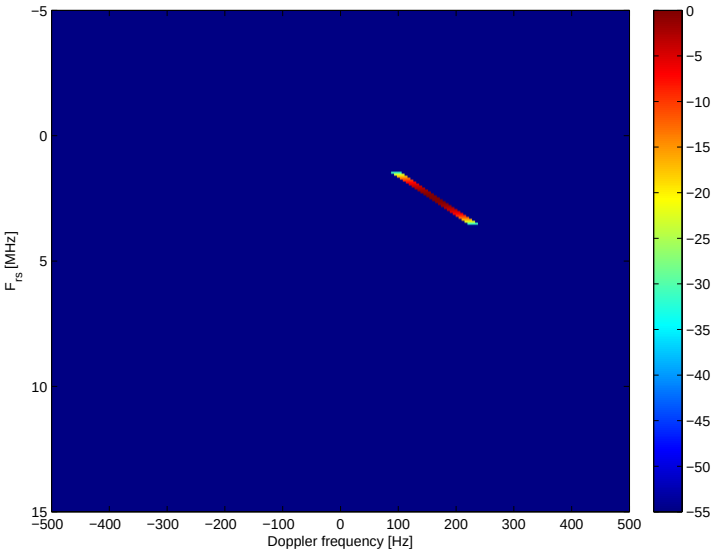

(c) Result from acquisition of data in Figure 3.2(a) using the pulse shown in Figure 3.1

Figure 3.2: The ultrasound pulse truncates signal from moving tissue in 2D power spectrum. The y- and x-axis show radial and Doppler frequency, respectively.

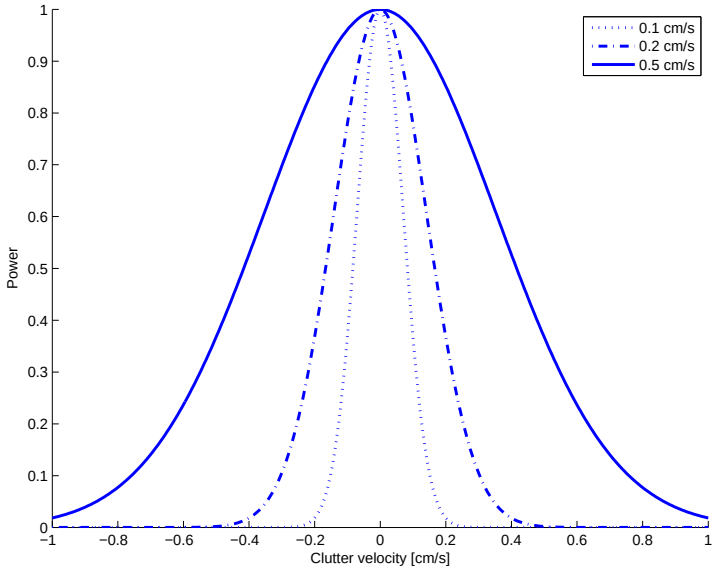

Figure 3.3: Simulation of clutter by Gaussian-shaped power signal along Doppler frequency. Here shown with different bandwidths mapped onto the corresponding velocity axis, where a given rms-bandwidth corresponds to axial velocity.

3.2.3 Signal from clutter

The clutter signal, either signal from reverberations or strong reflectors in side-lobes, contains velocity information from a region of no interest and thus distorts the velocity estimation. Signal from reverberations is near stationary and caused by non or slowly-moving tissue, i.e. from the chest wall, while a strong reflector in a side-lobe can have a high variation in velocity over in the case a heart valve falls into a side-lobe. The simulation of clutter will for simplicity be of the type from reverberations. As the unwanted movements from the hand of the transducer operator is present, it is plausible to assume this signal to contain normal distributed velocity information with zero mean, which is realised by means of a Gauss shaped signal along the Doppler frequency around 0 Hz. The clutter bandwidth B_{cl} is chosen as the rms-bandwidth of the Gauss curve and related to clutter velocity v_{cl} through Eq. (3.1):

$$B_{cl} = \frac{2 f_c v_{cl} \cos(\phi)}{c} \tag{3.1}$$

Here f_0 is the centre frequency of the transducer pulse, ϕ the intersection angle between the clutter and the ultrasound beam and c is the speed of sound in tissue.

Figure 3.3 shows the clutter signal along the Doppler frequency domain

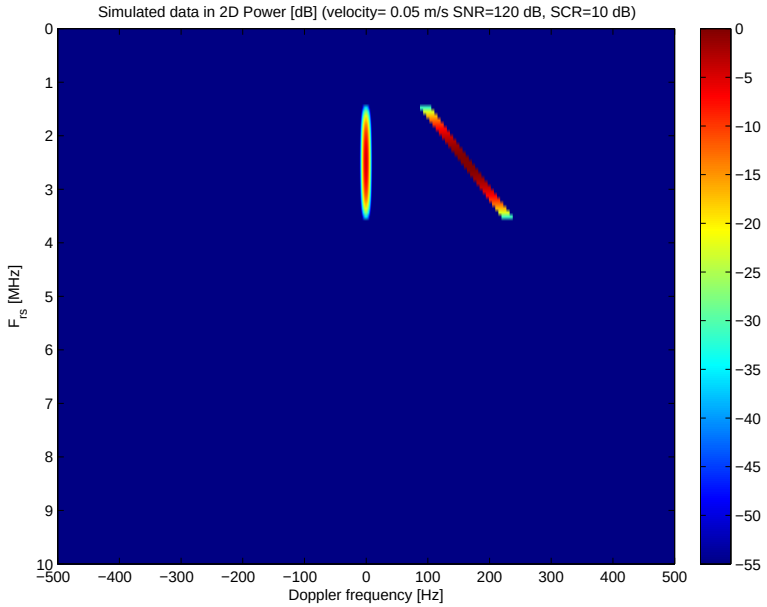

Figure 3.4: Clutter signal added to the signal from moving tissue in 2D power spectrum. The signal-to-clutter ratio is 10 dB.

for three different values of v_{cl}. In this work, the clutter movements are limited by setting v_{cl} equal to 0.1 cm/s.

The clutter signal together with signal from moving tissue in the 2D power spectrum can be found in Figure 3.4. The two signals were truncated separately by the ultrasound pulse in Figure 3.1 before addition. Here the moving tissue has an axial velocity of 5 cm/s and the signal-to-clutter ratio is 10 dB. This ratio was computed on the signals after the receive filter in Figure 3.1 was applied, giving the true ratio in the received signal. A negligible amount of clutter is achieved by setting SCR to 120 dB.

3.2.4 Signal loss and thermal noise

The presence of thermal noise in true acquisition systems is due to losses, both in the transducer and in the signal transmission to receiver amplifier, and noise in the receive amplifier. Thermal noise is white and therefore easily modeled with a constant over the full 2D power spectrum. The signal from thermal noise is then scaled by calculating signal-to-noise ratio (SNR) after the receive filter is applied to the noise signal as well as the signal from moving tissue. Figure 3.5 shows the addition of thermal noise to the signals from moving tissue and clutter after the receive filter was applied. Here, the signal-to-noise ratio is 10 dB.

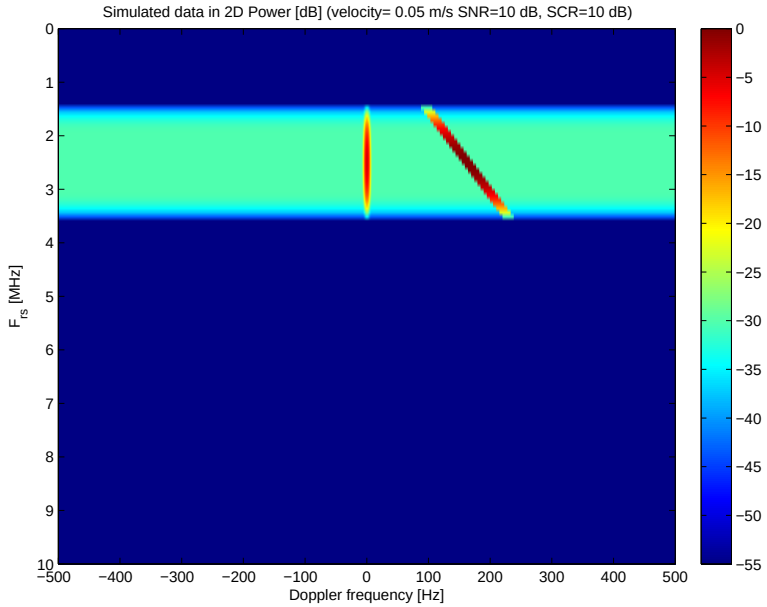

Figure 3.5: Thermal noise added to the signal from moving tissue and clutter in 2D power spectrum. The signal-to-clutter and signal-to-clutter ratios are both 10 dB.

3.2.5 Statistic Gaussian signal

The back-scattered amplitudes in an ultrasound signal from human tissue follows a Gaussian distribution [5]. The simulated signal is made statistic by multiplication with a random signal in the 2D Fourier domain. If the amplitude distribution of the random signal follows a Gaussian distribution, the amplitude distribution of the resulting signal becomes Gaussian as well. Figure 3.6 shows the resulting Gaussian simulated signal in 2D power spectrum, when a complex Gaussian random signal with zero mean and unit standard deviation was used for multiplication. The resulting signal is statistic Gaussian and complex, therefore, and the IQ-data is obtained by 2D inverse Fourier transform.

3.2.6 Aliasing

Aliasing occurs when the sampling frequency is less than half of the highest frequency component in the signal being sampled [10, Chapter 4.2]. In ultrasound acquisition aliasing occurs along the Doppler frequency in the received signal if scatterers move faster than the Nyquist velocity, relatively to the transducer. Aliasing can be introduced in the simulated signal through decimation along slow time in RF-domain, and Figure 3.7 shows the consequence of aliasing in the 2D power spectrum. Figure 3.7(a) shows a signal

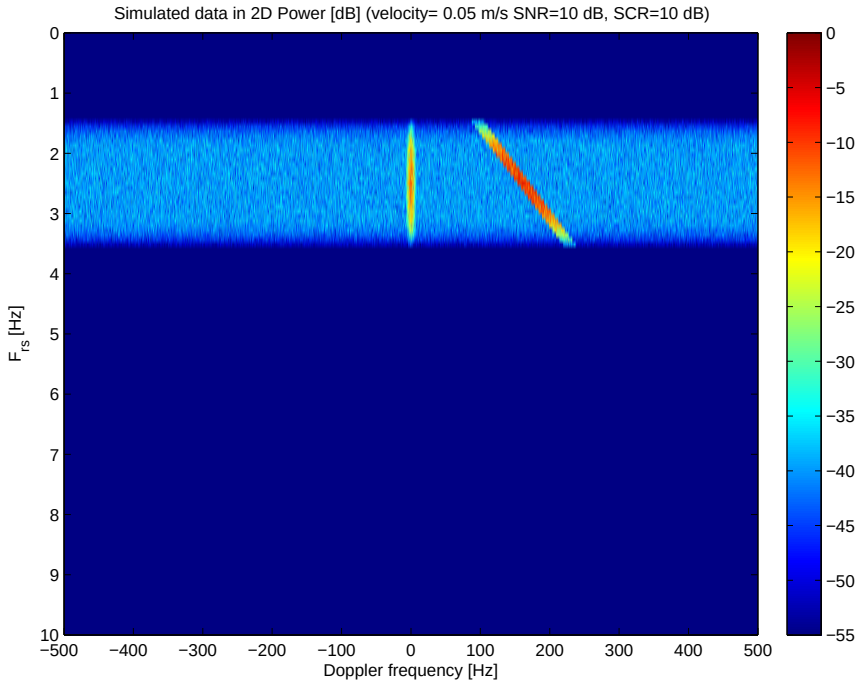

Figure 3.6: Received simulation signal made statistic Gaussian.

from tissue moving with axial velocity 8 cm/s with a PRF of 1600 Hz, while Figure 3.7 (b) shows the same signal decimated a factor of 4, yielding a new PRF of 400 Hz.

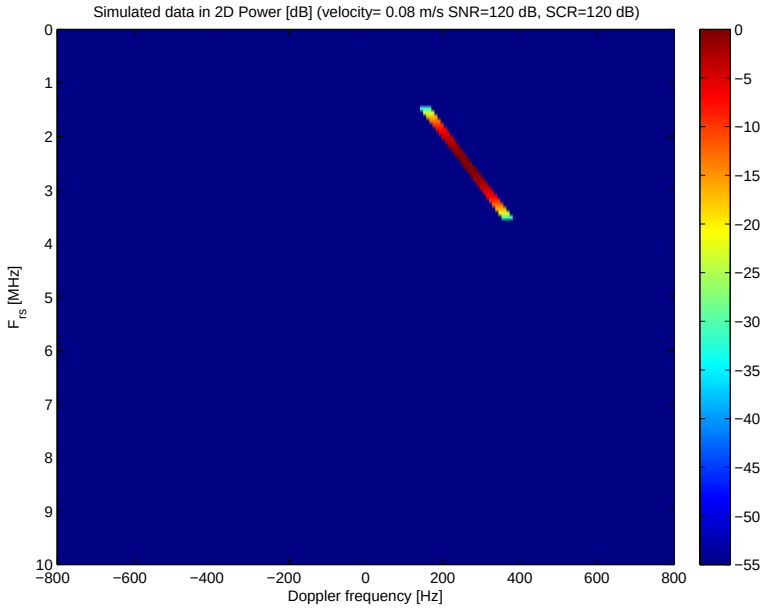

(a)

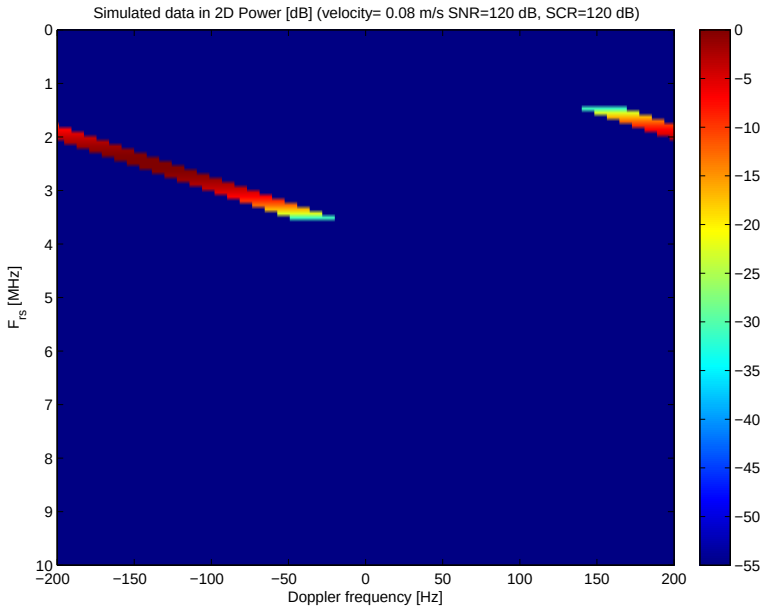

(b)

Figure 3.7: Signal from moving tissue decimated in RF-domain to introduce aliasing to the simulation model. The axial velocity of moving tissue is 8 cm/s, and the PRF is: a) 1600 Hz b) 400 Hz.

3.3 Simulation model verification

The simulated received signal is intended to have certain properties determined by the simulation parameters. Spectral analysis of the received signal is carried out and compared to the power spectrum of the effective pulse found in Figure 3.1. For this purpose, simulated signal from moving tissue and clutter in addition to thermal noise is obtained by the simulated acquisition system with a pulse centre frequency of 2.5 MHz and bandwidth B_{-6dB} of 1.1 MHz. The axial velocity of the moving tissue is 5 cm/s, while SCR and SNR both are set to 10 dB. A hamming window is weighted along the radial samples before estimation of the spectrum in order to reduce side-lobe effects in the estimated spectrum.

Additionally, the RF-signal will be inspected to verify the addition of thermal noise, clutter and aliasing.

3.4 Simulation model set-up

For the simulation model to be realistic, the received simulated signal is desired to have similar properties to a signal acquired with a real transducer in a real environment. The following subsections describes the determination of different parameters in terms of achieving a realistic simulation model.

3.4.1 Pulse centre frequency and bandwidth

In the following, experimental data recorded with GE Vingmed Ultrasound's Vivid 7 is used as a reference for the simulation data, in order determine the centre frequency and bandwidth to be used for simulations. Instead of estimating the centre frequency and bandwidth of the experimental data, another approach is taken where the simulation data spectrum will be adapted to the spectrum of the experimental data, in a mean-square-error sense, by varying the centre frequency and the bandwidth. The experimental data of a healthy human heart is acquired by the M3S transducer, with pulse centre frequency 2.5 MHz and a pulse length of 3 periods. Figure 3.8 shows one frame of recorded data visualised through GCMat. The full data set will be used for the estimation of the spectrum, consisting of 181 radial samples, 32 lateral samples and 24 frames. However, the image does contain regions of blood, but the contribution made to the estimated power spectrum is considered insignificant as signal from tissue is much stronger than blood. A hamming window is weighted along the radial samples before estimation in order to reduce the side-lobe effects on the spectrum.

The simulated signal used for adaption is the signal shown in Figure 3.6, having SCR and SNR equal to 10 dB and a signal from tissue moving at 5 cm/s towards the transducer.

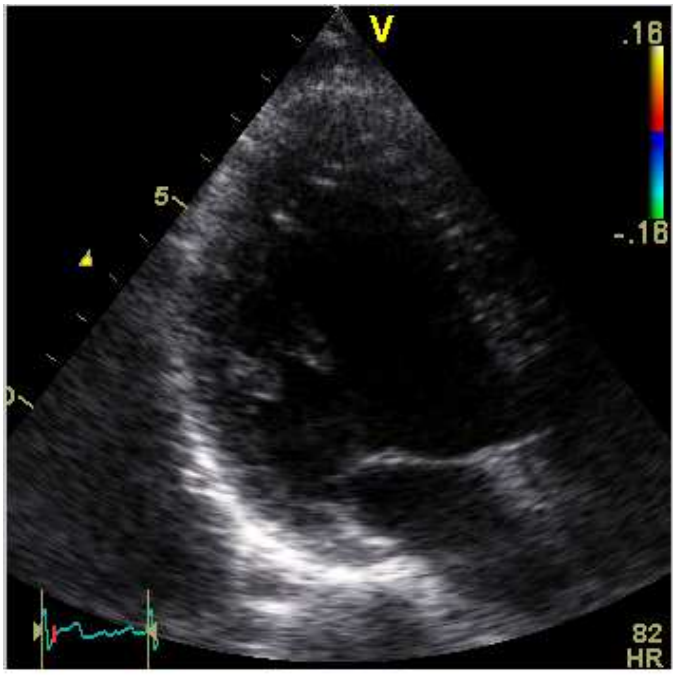

Figure 3.8: B-mode image of the left ventricle in a healthy human heart. The full data set is used for spectral analysis.

3.4.2 Pulse beam width

The ultrasound beam width D_F at a specific depth d can be found given the aperture D and centre frequency f_0 from Table 3.1, where the corresponding $F_\#$ is given by

$$F_\# = \frac{d}{D}. \tag{3.2}$$

Considering a plausible depth for measuring tissue velocities to be 8 cm, the beam width D_F is determined to

$$D_F = F_\# \lambda = \frac{0.08 \cdot 1540}{0.022 \cdot 2.5 \cdot 10^6}\ cm = 0.22\ cm. \tag{3.3}$$

3.4.3 Temporal signal length

Choosing signal length is related to repeatability of the experiments as the deviation between experiments decreases with increased number of slow-time samples. To achieve practical simulation time for the experiments, 8192 is considered a reasonable compromise between simulation time and deviation from experiment to experiment. When using PRF equal to 1 kHz, the slow-time signal duration then becomes roughly 8 seconds.

The temporal signal length should be sufficiently longer than the signal correlation time. Due to its low-pass characteristics, the signal from clutter

will have the longest correlation time T_{cl} within each range bin. The clutter correlation time T_{cl} is estimated by the rms-bandwidth B_{cl} inverse, where inserting the parameters from Table 3.2 into Eq. (3.1), when v_{cl} is 1 mm/s, yields B_{cl} equal to 2.83 Hz. Furthermore, the clutter correlation time is found by $T_{cl} = \frac{1}{2.83 \text{ Hz}} = 0.35$ sec – considerably shorter than the temporal signal length in simulations using 8192 samples and PRF set to 1 kHz.

Repeatedly velocity estimation on simulation data produced with the same parameters allows to measure the uncertainty in experiments based on 8192 temporal samples. In order to put the result in context with other signal lengths, N estimations are brought out on slow-time samples ranging from 1024 to 10240 in steps of 1024. The parameter set-up for the simulation model used for this purpose is listed in Table 3.2, while 5 cm/s tissue motion is simulated when both SCR and SNR are set to 10 dB. The simulation data applied to the autocorrelation estimator, described in Section 3.7.2, yields a variance estimate $\hat{\sigma}^2_{i,l}$ for each simulation i for each signal length l. The mean estimated standard deviation for each signal length l is then given by

$$\bar{\hat{\sigma}}_l = \sum_{i=1}^{N} \frac{\sqrt{\hat{\sigma}^2_{i,l}}}{N}, \tag{3.4}$$

where N is the number of simulations for each signal length, set to 300. The corresponding variance estimate is further obtained from

$$\text{std}(\hat{\sigma}_l) = \sqrt{\frac{1}{N-1} \sum_{i=1}^{N} (\sqrt{\hat{\sigma}^2_{i,l}} - \bar{\hat{\sigma}}_l)^2}. \tag{3.5}$$

Finally, the ratio between the standard deviation and the mean estimate of the standard deviation is found by

$$\Gamma = \frac{\text{std}(\hat{\sigma}_l)}{\bar{\hat{\sigma}}_l}. \tag{3.6}$$

3.4.4 Parameter set-up

Table 3.2 lists the typical set-up of essential parameters for the simulation environment outlined in this text. In experiments where the value is changed for some reason, that will be clearly stated in the text, if not evident from the experiment itself.

3.5 Using the simulation model

The simulation model developed in this work carry out the opportunity to assess the process of velocity estimation in a controlled environment and intends to supply the velocity estimators with realistic data. The model allows

Parameter	Value
Radial samples	512
Temporal samples	8192
Center frequency, f_0	2.32 MHz
Bandwidth, BW_{-6dB}	0.7 MHz
Radial sampling frequency, f_{rsRF}	40 MHz
Pulse repetition frequency, PRF	1 kHz
Speed of sound, c	1540 m/s
Intersection angle, ϕ	20°
Beam width	2.2 mm

Table 3.2: Simulation model parameter set-up

for separate investigation of several aspects, related to signal or system, in order to assess their effect on the velocity estimates. These investigations aim to point out one or more candidates that prevent the modified autocorrelation method from superior performance on experimental data, compared to the conventional method. Evaluation of the velocity estimators with respect to statistic properties like bias and standard deviation is carried out in order to do this selection. Motivation for investigation of each aspect and relation to true acquisition is described below.

3.5.1 Signal-to-noise ratio

As thermal noise is modeled as white noise it increases the randomness in the received signal. In a true acquisition system low SNR can be compensated for by increasing the power of the ultrasound pulse transmitted by the transducer. However, ultrasound exposure to human tissue is, for safety reasons, limited by some intensity measures [5]. The investigation of signal-to-noise ratio will be in the range from 5 to 25 dB.

3.5.2 Signal-to-clutter ratio

Acoustic noise signal from clutter directly affects the frequency content along the Doppler frequency, where the phase-shift estimators operate in order to estimate the mean frequency. Based on the assumption that clutter has low velocity, it can be reduced by means of a high-pass filter applied along the Doppler frequency. Section 3.7.1 describes the clutter filter used in this work. A separate investigation of the clutter filter effects is carried out. The investigation of signal-to-clutter ratio will be in the range from 0 to 25 dB.

3.5.3 Aliasing

When the velocity signal exceeds the Nyquist limit, the velocity signal is wrapped around from positive to negative velocity, or vice versa. To cope with this, a simple unwrap algorithm is applied to the phase angle estimates. Since working with simulation data means working with constant velocity, the applied algorithm unwraps the phase angles in the estimated slow-time correlation function of lag one $R(0,1)$, if the sign is the opposite of the sign of the velocity simulated. The cross-correlation estimator is in principle not affected by aliasing, but for reasons to be clarified in Section 3.7.3, the maximum detectable velocity is parametrised as v_{max} and equal to the Nyquist velocity by default. In this experiment, v_{max} is set to two times the Nyquist velocity. As this should allow for detection of velocities up to two times the Nyquist velocity for all three estimators, this is also the range for investigation of aliasing.

3.5.4 Angle dependency

The transit time, which is dependent on angle of intersection between moving scatterers and the ultrasound beam, is inversely proportional to the bandwidth of the signal from moving tissue. To deal with angle dependency, the ultrasound transducer should be held in the same plane as the scatterers of interest move along. The investigation of angle dependency will be in the range from 1 to 45 degrees.

3.5.5 Pulse bandwidth

As seen in the section describing the simulation model, the choice of pulse bandwidth limits the amount of spectral information available to the velocity estimators. In a true acquisition system the choice of bandwidth is done by setting the pulse length, as they are inversely proportional to each other. Using short pulse lengths give high spatial resolution, but compromises the received signal-to-noise ratio. The investigation of the -6 dB peak bandwidth B_{-6dB} will be in the range of 0.25 MHz to 1.65 MHz.

3.6 Experimental data acquisition

The velocity estimators are applied to experimental data acquired by GE Vingmed Ultrasound's Vivid 7 for in-vivo investigation. Septum of a healthy human heart is captured in narrow acquisition, using the set-up listed in Table 3.1 with 16 lateral beams. This resulted in 270 frames per second. In order to focus on the difference in variance when comparing AM and MAM, the bias effect in AM is reduced by replacing the demodulation frequency f_{dem} in Eq. (2.29) with the mean estimated radial frequency $\hat{f}_0$ for the given range bin, defined by Eq. (2.30).

Analysis comprise investigation of difference in velocity estimation Δv between the two phase-shift estimators considered in this work, AM and MAM, given by

$$\Delta v = v_{AM} - v_{MAM}. \tag{3.7}$$

Here, Δv is zero in mean, due to the aforementioned compensation of demodulation frequency f_{dem}. Standard deviation of the difference velocity signal $\hat{\sigma}_{\Delta v}$ over an interval with N temporal samples, is then estimated as

$$\hat{\sigma}_{\Delta v} = \sqrt{\frac{1}{N-1}\sum_{i=1}^{N}\Delta v_i^2}. \tag{3.8}$$

The estimation will be made in an interval appropriate for comparison with results from simulations. That is, comparison of the estimated standard deviation for the difference signal $\hat{\sigma}_{\Delta v}$ with the expected difference from simulations with similar parameter set-up, intends to look into the correlation in error estimation done by AM and MAM.

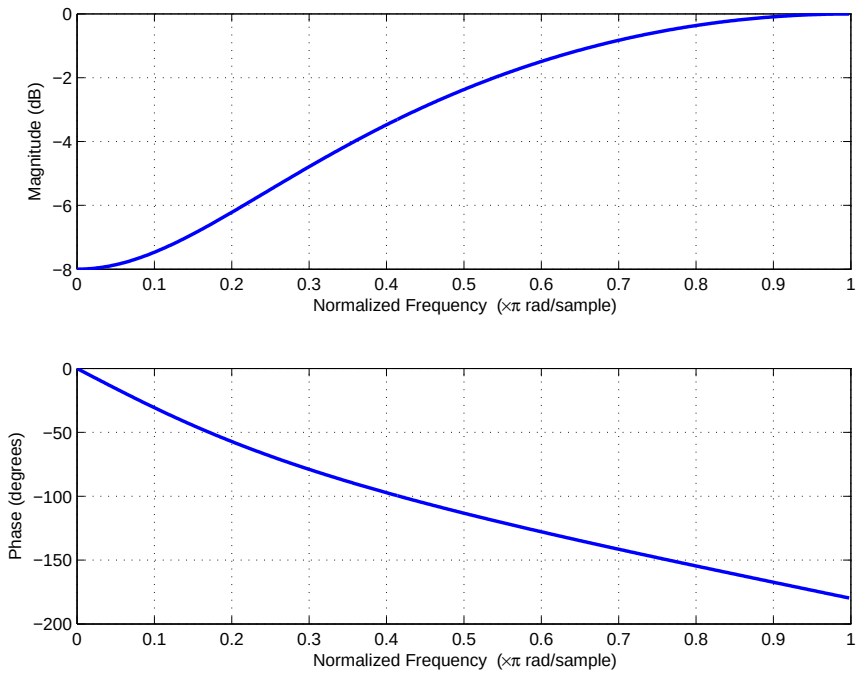

Figure 3.9: Magnitude and phase of the 1. order FIR filter for clutter removal.

3.7 Tissue velocity estimation

Since the implementation of tissue velocity estimation is adopted from previous work not published, a description will be given in this text to form a whole. The velocity estimators assume a 2D array of IQ-data $x(m, n)$, where row and column correspond to fast-time and slow-time, respectively. This data set constitute the basis for each velocity estimate. Throughout this work, the number of slow-time samples are set to 3, while the number of fast-time samples are set to a value corresponding to 6 mm in radial distance. These values determines the temporal and spatial averaging, respectively.

3.7.1 Clutter filtering

Prior to velocity estimation, the IQ-data are filtered to reduce the amount of clutter in the signal. By assuming the clutter signal to only contain low Doppler frequencies, the clutter removal filter is applied along the slow-time dimension. Due to the few temporal samples available, a FIR filter of 1st order is applied, and its magnitude and phase is shown in Figure 3.9. As the filter also attenuates the signal from slowly-moving tissue within the region of interest, it is a trade-off between velocity estimation and artifacts from reverberations and strong reflecting objects in a side-lobe. The filter

operation reduces the number of temporal samples in the signal with one, thus 2 temporal samples are available to the velocity estimators.

3.7.2 Autocorrelation methods

In order to estimate tissue velocities, the conventional autocorrelation method (AM) employs slow-time correlation only, while the modified autocorrelation method (MAM) makes use of both fast-time and slow-time correlation. Given the IQ-data in $x(m,n)$ the two-dimensional correlation function is defined as [12]

$$R(m',n') = \sum_{m=0}^{M-m'-1} \sum_{n=0}^{N-n'-1} x^*(m,n)x(m+m',n+n'), \tag{3.9}$$

where m and n are radial and temporal index, respectively. The implementation of this function in MATLAB is shown below, where the two input parameters correspond to m' and n' in Eq. (3.9).

```
function R=getautocorr(segmat,m,n)
%The function computes the 2D autocorrelation R(m,n) on the
%matrix given in 'segmat'. The input parameters m and n decide
%the lags to be computed.

[M N]=size(segmat);
R=0;
for idxm=1:M-m
    for idxn=1:N-n
        R=R+(conj(segmat(idxm,idxn)).*segmat(idxm+m,idxn+n));
    end
end
```

Both methods use this function to obtain the slow-time correlation function at lag one $R(0,1)$. AM estimates the velocity directly using Eq. (2.29), while MAM obtains $R(1,0)$ in order to estimate the received centre frequency $\hat{f}_0$ using Eq. (2.30), prior to estimation of velocity by Eq. (2.31).

For both of the autocorrelation methods, the number of fast-time samples determines the spatial averaging, which reduce the overall estimation variance. Although not considered in this work, spatial averaging compromises the spatial resolution of the velocity estimates, thus a compromise is made when the number of fast-time samples is set to a value corresponding to 6 mm in range.

3.7.3 Cross-correlation method

As the cross-correlation method estimates velocities on samples in the RF-domain, the IQ-data are brought into RF-domain prior to estimation. In

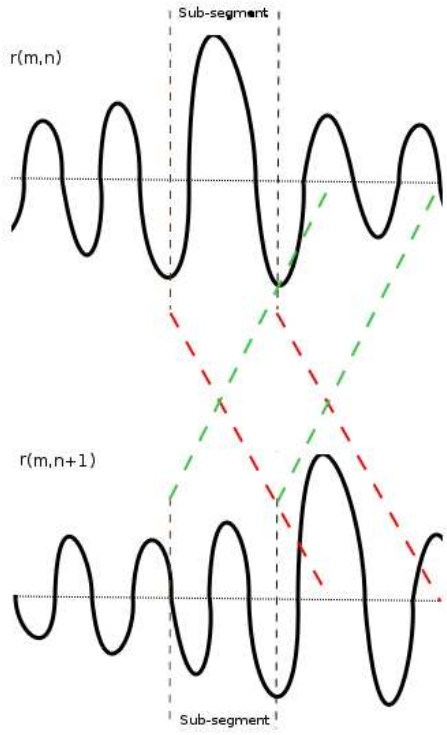

Figure 3.10: Estimation of cross-correlation from two subsequently received RF-pulses using sub-segments.

order to avoid possible edge-effects, the conversion is applied along the full RF-line, before the RF-signal $z(m,n)$ is achieved. Here, the data in $z(m,n)$ is spatially equivalent to $x(m,n)$, but the number of fast-time samples is a factor I times higher than that of $x(m,n)$, where I is the interpolation factor in the conversion from IQ-data to RF-data, hence, the cross-correlation method is computationally more demanding than AM and MAM.

As previously mentioned, the number of slow-time samples is 2. The cross-correlation estimate of the two available segments of the RF-line is carried out using Eq. (2.34). In order to reduce the considerably high probability of global errors [5, 12], the maximum lag l' calculated in Eq. (2.34) is constrained to a number N_{maxlag} lower than N_S. This is realised by correlation of sub-segments in the first RF-line, with equally sized, overlapping sub-segments of the second RF-line. By using the same procedure on sub-segments of the second RF-line, the two cross-correlation estimates are averaged to achieve lower estimation variance. This concept is illustrated in Figure 3.10. The resulting cross-correlation estimate $\hat{R}_{12}(l')$ then have values in range of $[-N_{maxlag}, N_{maxlag}]$, where the highest detectable velocity v_{max} is related to N_{maxlag} by

$$N_{maxlag} = \left\lceil \frac{v_{max} 2 f_{rsRF}}{c \cdot PRF} \right\rceil. \tag{3.10}$$

Here f_{rsRF}, listed in Table 3.2, is the fast-time sampling frequency of the RF-signal. In this work, v_{max} is set to the Nyquist velocity by default.

Furthermore, the cross-correlation estimate has its maximum value at l_m. Due to quantization of possible lags, the precision of the velocity estimate is increased by parabolic curve fitting around the maximum value. The interpolated value is then given by [5, 12]

$$l_{int} = \frac{1}{2} \frac{\hat{R}_{12}(l_m - 1) - \hat{R}_{12}(l_m + 1)}{\hat{R}_{12}(l_m - 1) - 2\hat{R}_{12}(l_m) + \hat{R}_{12}(l_m + 1)} + l_m. \tag{3.11}$$

Estimation of tissue velocities by CCM is then given by

$$v_{int} = \frac{c \cdot l_{int}}{2 f_{rsRF}} PRF. \tag{3.12}$$

The implementation of the cross-correlation estimator using parabolic fitting was verified in aforementioned work not published.

Chapter 4

Results

This chapter presents the results of this work according to the procedure outlined in the previous chapter. This comprise verification and adaption of the simulation model, effects from clutter filtering, and tissue velocity estimation of simulated and experimental data.

4.1 Simulation model verification

4.1.1 Frequency analysis

Frequency analysis of the simulated received signal is carried out in order to verify the simulation model developed in this work. Figure 4.1 shows the estimated power spectrum of the received signal and the effective pulse of the simulated transducer in solid and dashed lines, respectively. For this comparison, simulated signal from tissue, moving at 5 cm/s towards the transducer, is acquired by a pulse with centre frequency f_0 of 2.5 MHz and -6 dB peak-value bandwidth B_{-6dB} of 1.1 MHz. The normalized spectra are shown in decibel scale.

4.1.2 RF-domain analysis

Thermal noise

The thermal noise was modeled as a white noise signal added to signals from moving scatterers and clutter in the Fourier power spectrum. Figure 4.2 shows simulated RF-signals. Here the signals contain velocity information from moving scatterers in addition to thermal noise. The scatterers are moving with an axial velocity of 5 cm/s and the intersection angle is 20°. The signal-to-noise radios are 120 and 0 dB in the upper and lower plot, respectively.

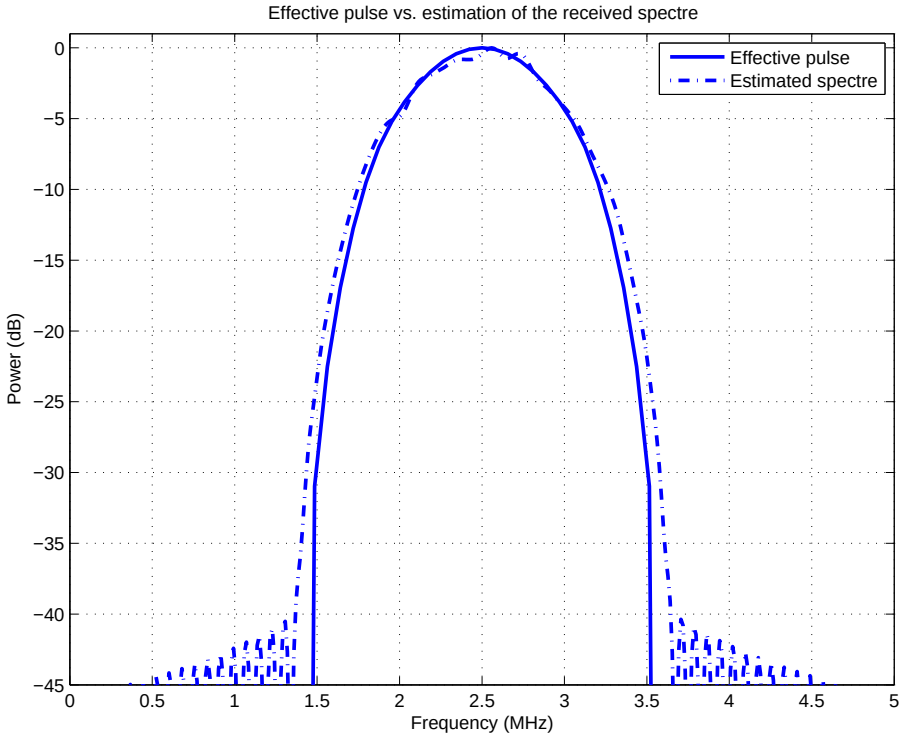

Figure 4.1: Estimated power spectrum of the simulated received signal versus power spectrum of the effective pulse simulated.

Clutter

The clutter was modeled as a low-pass component added to the signal from moving scatterers in the Fourier power spectrum. Figure 4.3 shows the simulated RF-signal, having information from moving scatterers and clutter. The moving scatterers intersect the ultrasound beam with an angle of 20° and the axial velocity is 5 cm/s. The signal-to-clutter ratios are 10 and 0 dB, in the upper and lower plot, respectively.

Aliasing

Aliasing was introduced to the model by decimating the RF-signal along the slow time dimension. Figure 4.4 shows simulated signals that have been decimated with different factors. The moving scatterers are intersecting the ultrasound with an angle of 20° having an axial velocity of 10 cm/s. Before decimation the PRF was 1500 Hz. The decimation factors are 1 and 4 in the upper and lower plot, respectively. This corresponds to Nyquist velocities of 22 m/s and 5.5 m/s.

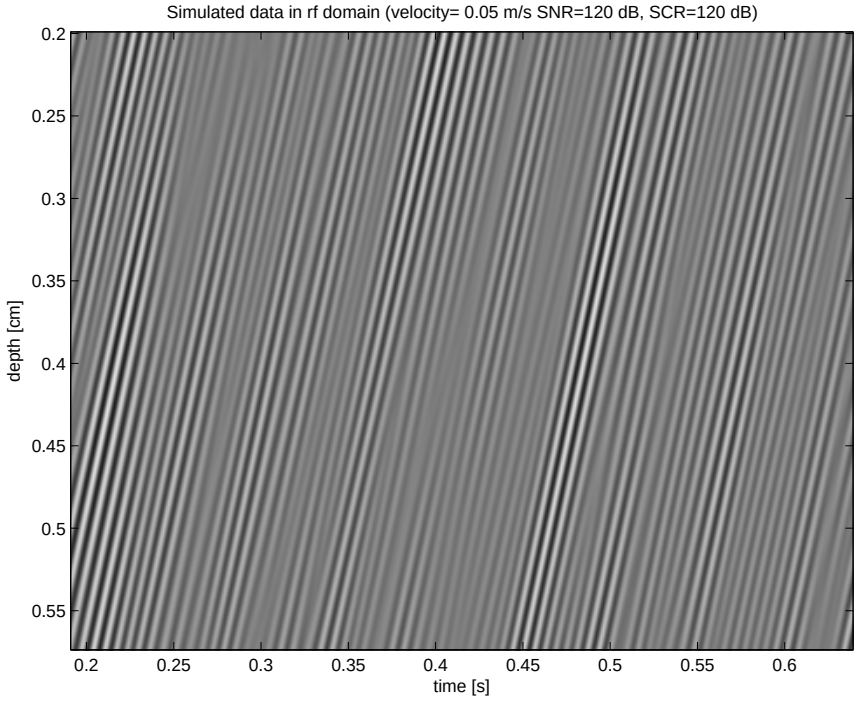

(a)

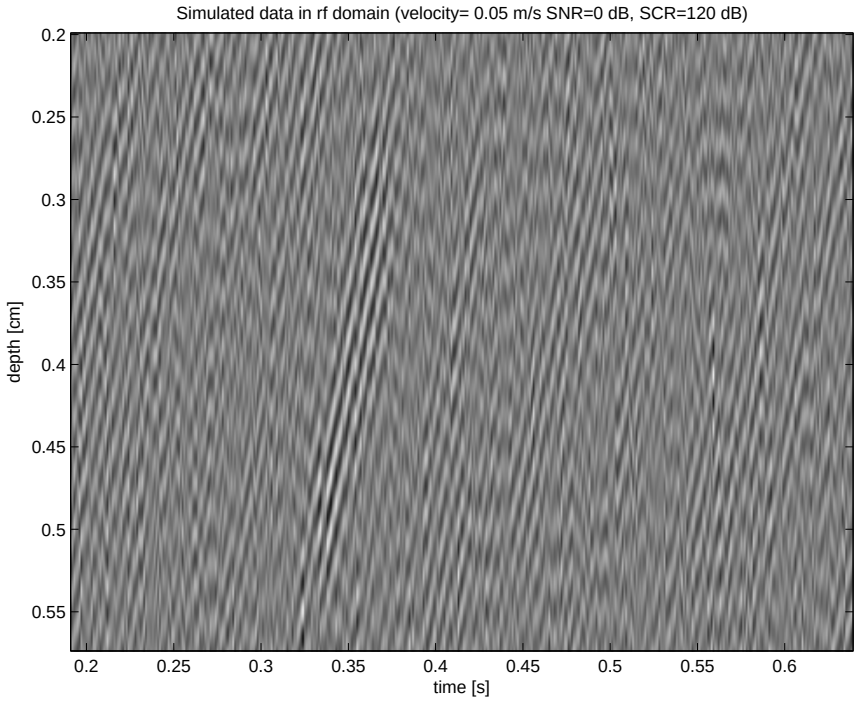

(b)

Figure 4.2: Simulated RF-signal with a SNR of a) 120 dB b) 0 dB

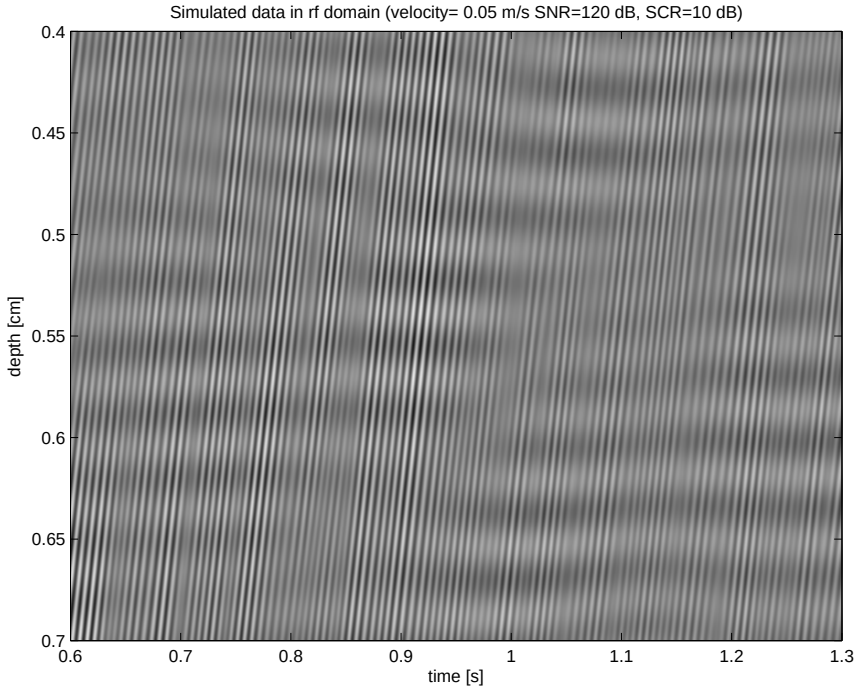

(a)

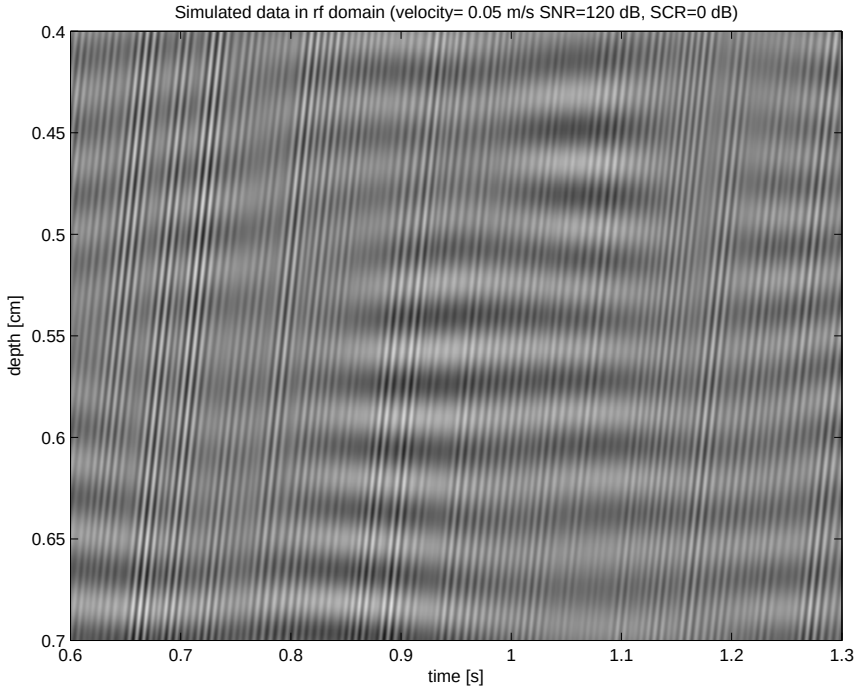

(b)

Figure 4.3: The simulated RF-signal with a signal-to-clutter ratio of a) 10 dB b) 0 dB

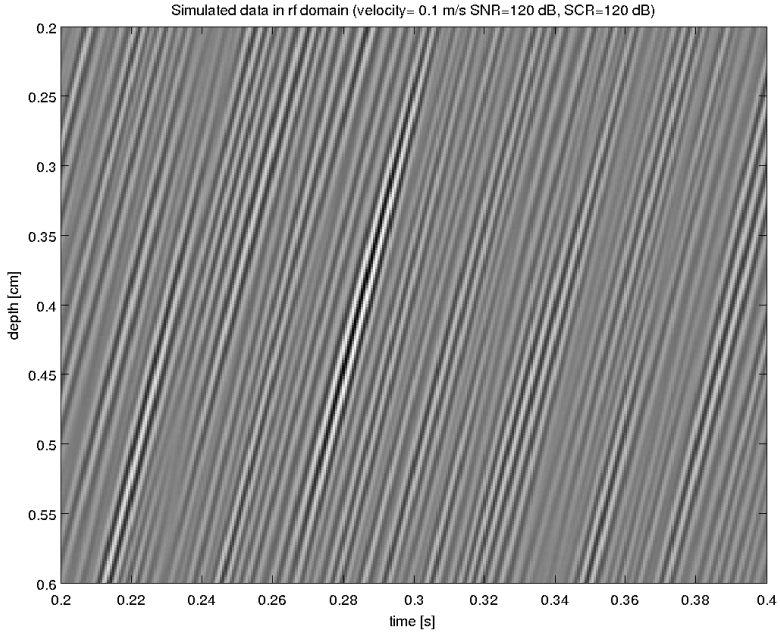

(a)

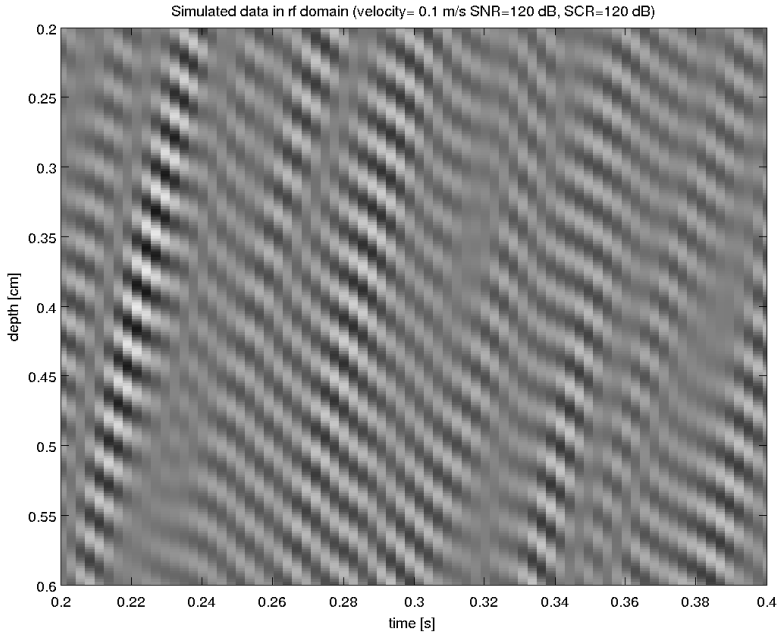

(b)

Figure 4.4: Simulated RF-signal from tissue moving at 10 cm/s decimated at a factor a) 1 b) 4. PRF is set to 1500 Hz before decimation.

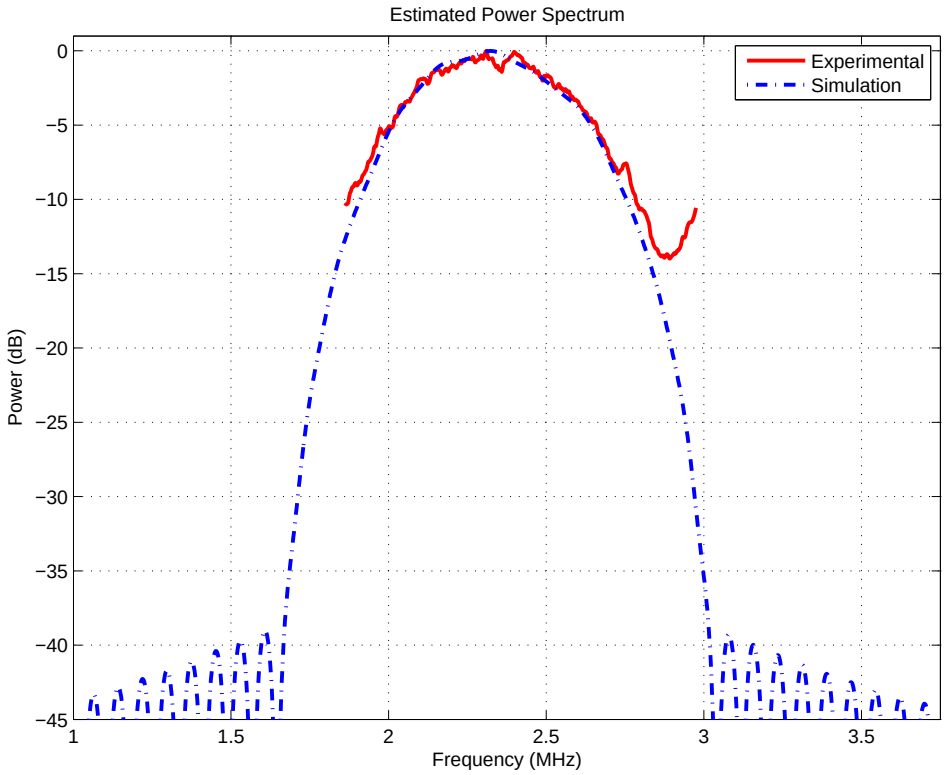

Figure 4.5: Estimated spectrum of experimental data shown in Figure 3.8 together with the best matching spectrum for the simulation data.

4.2 Simulation model set-up

4.2.1 Pulse centre frequency and bandwidth

Figure 4.5 shows the estimated power spectrum for the experimental data, in red, together with the best matching power spectrum for the simulation data, dashed in blue. Both spectra are normalised and shown in decibel scale. The centre frequency and -6 dB bandwidth for the simulation data was varied from 2.2 to 2.6 MHz and 0.3 to 1.1 MHz, respectively, where centre frequency equal to 2.32 MHz and bandwidth equal to 0.7 MHz gave the power spectrum with lowest mean-square-error difference to the estimated power spectrum from the experimental data. The presence of aliasing in the experimental data above 2.85 MHz limits the mean-square-error calculation interval to $1.90 - 2.85$ MHz.

4.2.2 Temporal signal length

Figure 4.6 shows the ratio of standard deviation of the estimated variance and its mean as a function of temporal signal length. For each number of

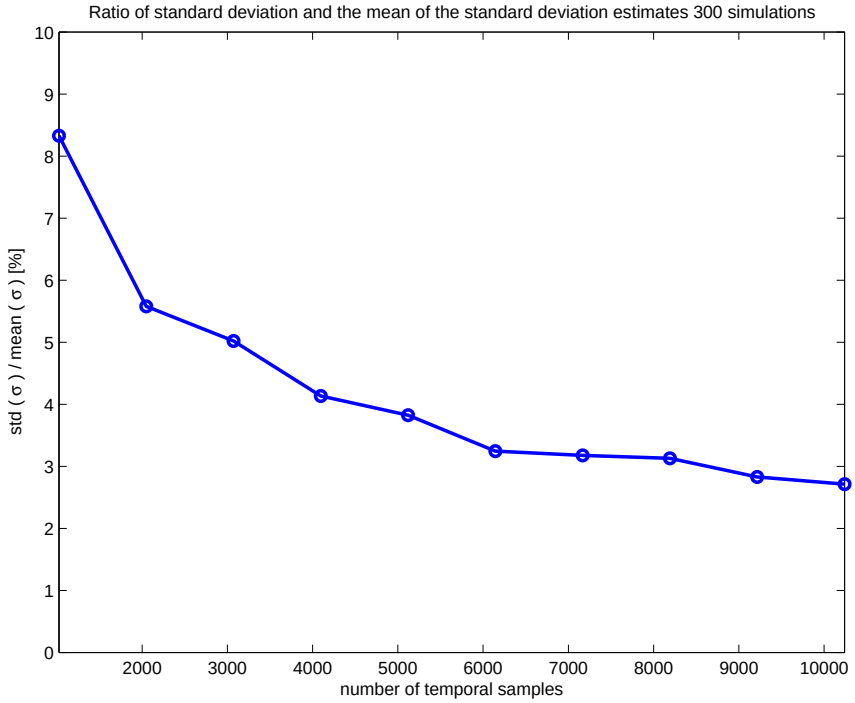

Figure 4.6: Ratio of standard deviation of the estimated standard deviation and its mean as a function of temporal samples. The calculations are based on 300 simulations for each signal length using AM for velocity estimation.

temporal samples (denoted with circles in the plot), data from 300 simulations were applied to AM for velocity estimation. The ratio is 3.1% when the estimation is based on 8192 temporal samples.

4.3 Clutter filtering

Prior to velocity estimation, a clutter filter is applied to the data. Figure 4.7 shows the two-dimensional power spectrum of the data before and after the one-dimensional 1st order FIR-filter in Figure 3.9 is applied along the slow-time samples. In the simulation data, signal from moving tissue simulates an axial velocity of 8 cm/s, while SCR and SNR are both set to 10 dB.

Using the same simulation model parameters, the data are applied to velocity estimation to investigate the effects from clutter filtering. For this purpose, the DC-level attenuation varies from 0 to 16 dB, and Figure 4.8 shows the mean estimated velocity and standard deviation as a function of attenuation.

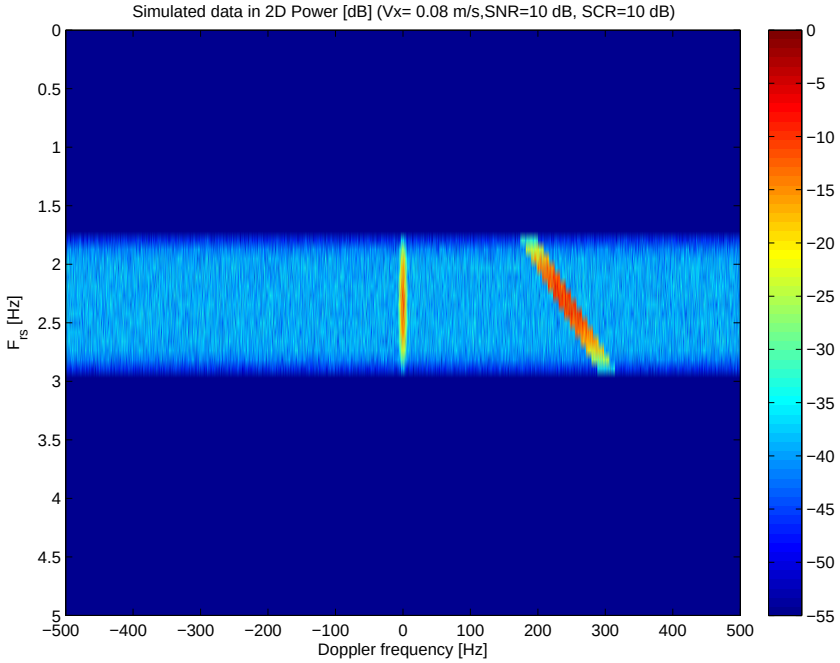

(a)

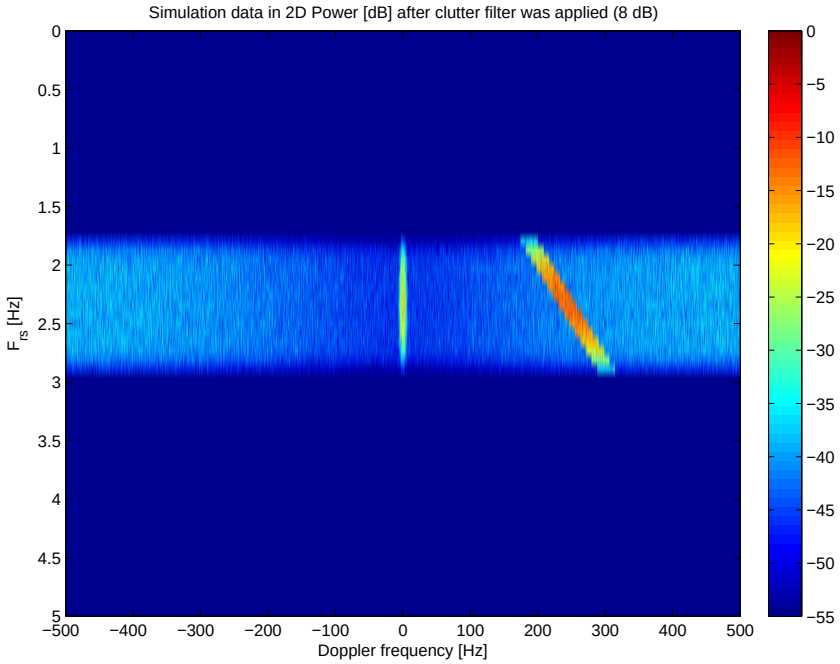

(b)

Figure 4.7: Showing the effect of clutter removal in the two-dimensional power spectrum. The clutter filter, a 1st order FIR filter with DC-level attenuation of 8 dB, is shown in Figure 3.9.

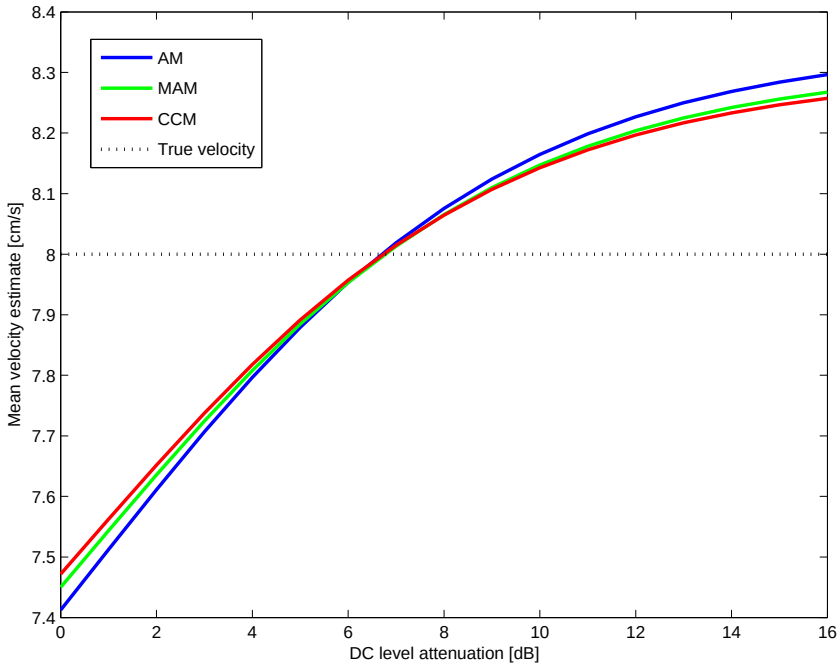

(a) Mean estimates

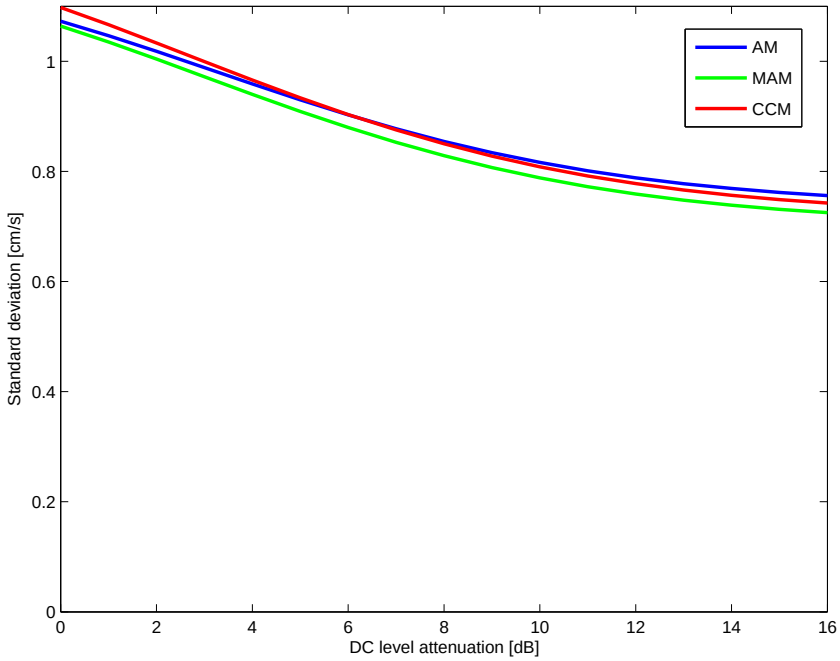

(b) Standard deviation

Figure 4.8: Mean estimated velocity and standard deviation as a function of DC-level attenuation for AM, MAM and CCM, respectively in blue, green and red.

4.4 Velocity estimation on simulation data

This section contains results obtained from velocity estimation on simulation data. The clutter filter is applied prior to velocity estimations for the following simulations.

4.4.1 Presence of thermal noise

By varying the amount of thermal noise in the simulation data, the effect thermal noise has in velocity estimation is investigated. Figure 4.9 shows the velocity bias and standard deviation for the three velocity estimators as a function of signal-to-noise ratio. The axial velocity of the moving scatterers is kept constant at 8 cm/s, and the intersection angle between the scatterers and the ultrasound beam is 20°.

4.4.2 Presence of clutter

By varying the amount of clutter in the simulation data, the effects from present clutter is investigated in terms of tissue velocity estimation. Figure 4.10 shows the mean velocity estimates and corresponding standard deviation for the three velocity estimators as a function of signal-to-clutter ratio. The axial velocity of the moving scatterers is kept constant at 8 cm/s, and the intersection angle between the scatterers and the ultrasound beam is 20°. For this experiment, the signal contain a negligible amount of thermal noise.

4.4.3 Aliasing

By decimating the simulation data along slow time in RF-domain, the Nyquist-velocity is reduced by the same factor. This introduces aliasing to the signal when the simulation data before decimation contained velocity information above the new Nyquist-velocity. To handle velocities above the Nyquist limit, a simple aliasing algorithm is applied to the two phase-shift estimators, making them able to cope with velocities up to two times the Nyquist-velocity. Correspondingly for the cross-correlation estimator, the parameter v_{max} in Eq. (3.10) is set to two times the Nyquist-velocity.

Figure 4.11 shows the velocity bias and standard deviation for the three velocity estimators as a function of axial velocity. In the simulation model, the PRF and decimation factor was set to 1500 Hz and 5, respectively, yielding an effective PRF of 300 Hz and Nyquist limit at 4.9 cm/s after decimation. Signal from clutter and thermal noise is negligible in this experiment.

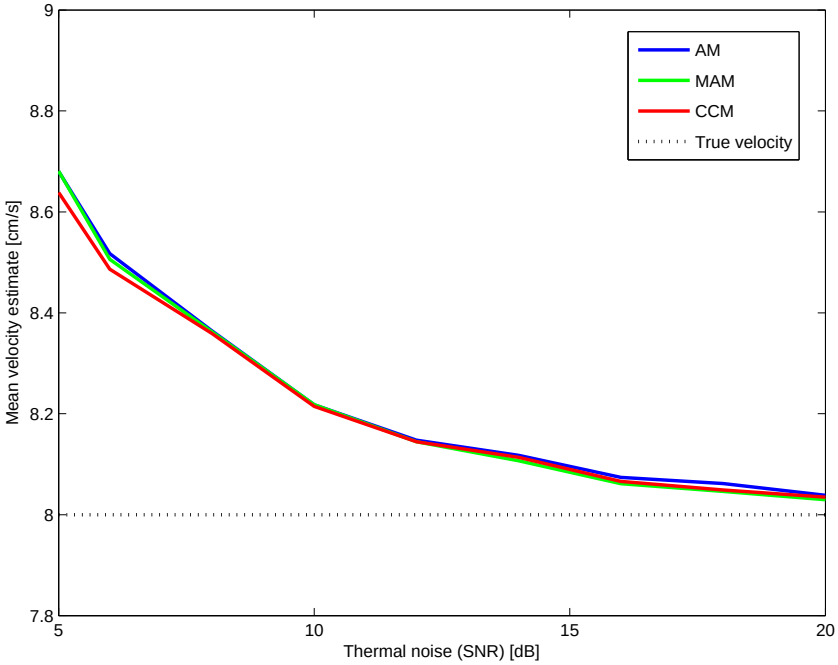

(a) Mean estimates

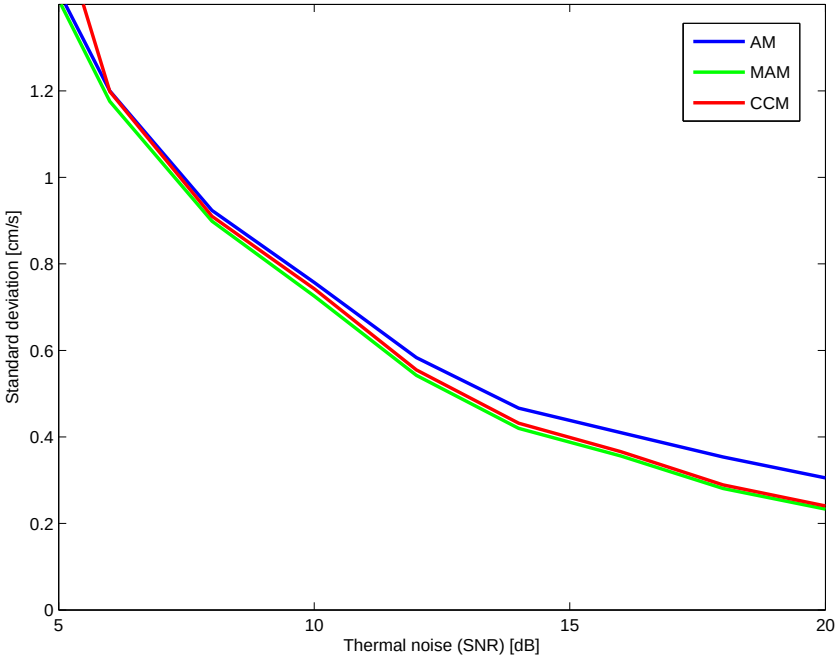

(b) Standard deviation

Figure 4.9: Mean estimated velocity and standard deviation as a function of signal-to-noise ratio using AM, MAM and CCM.

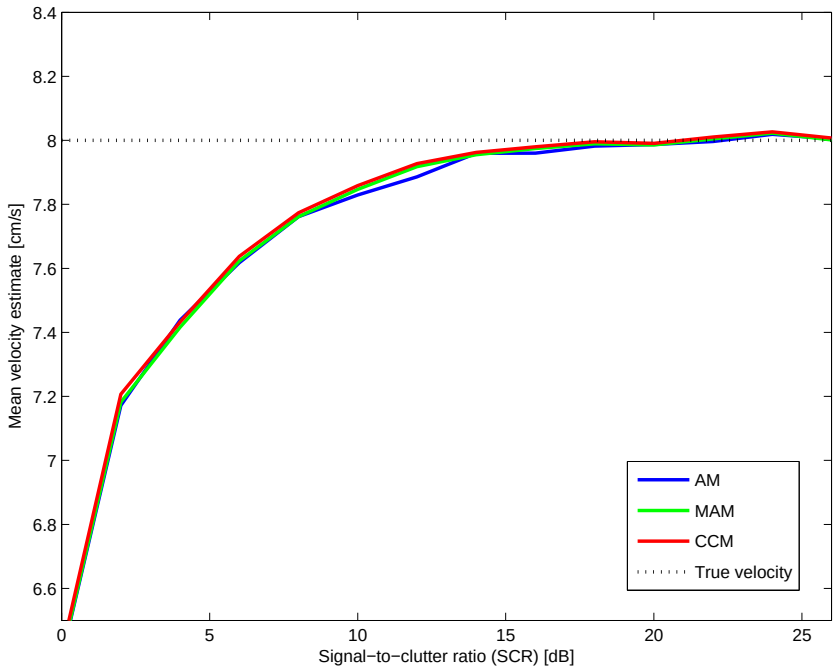

(a) Mean estimates

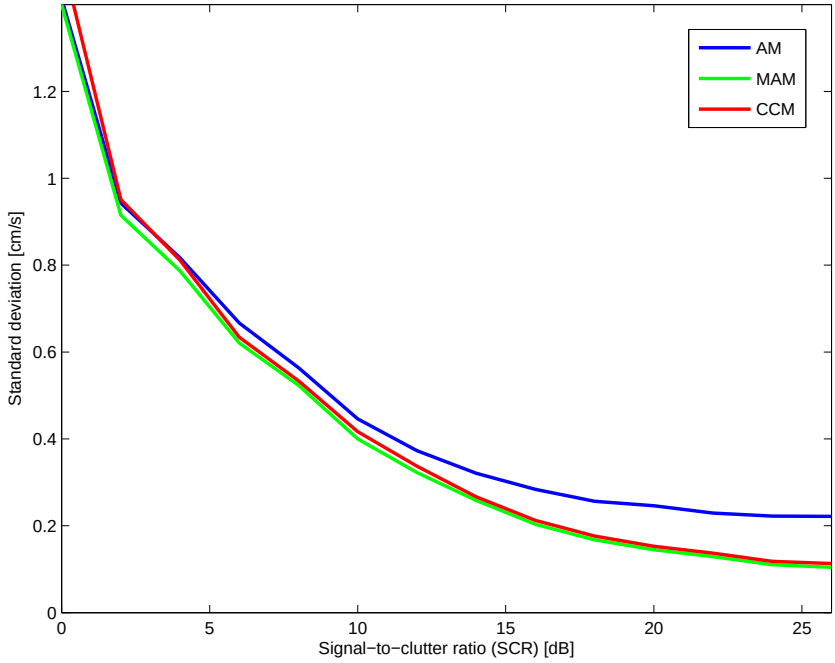

(b) Standard deviation

Figure 4.10: Mean estimated velocity and standard deviation as a function of signal-to-clutter ratio using AM, MAM and CCM.

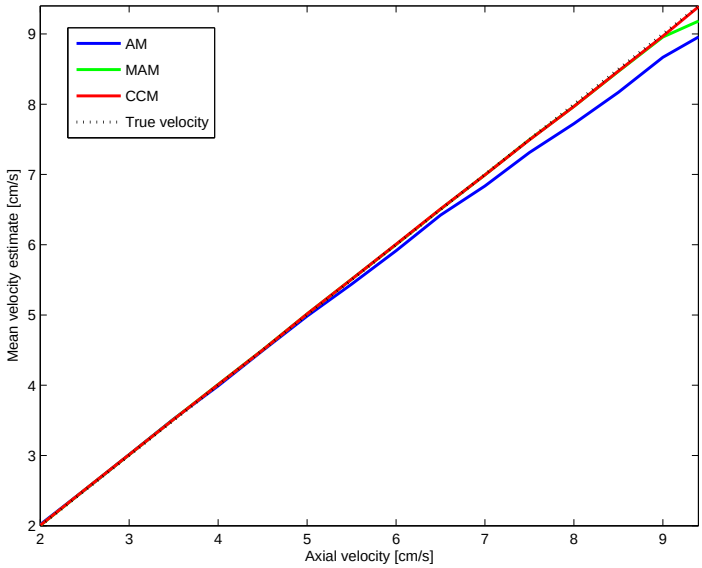

(a) Mean estimates

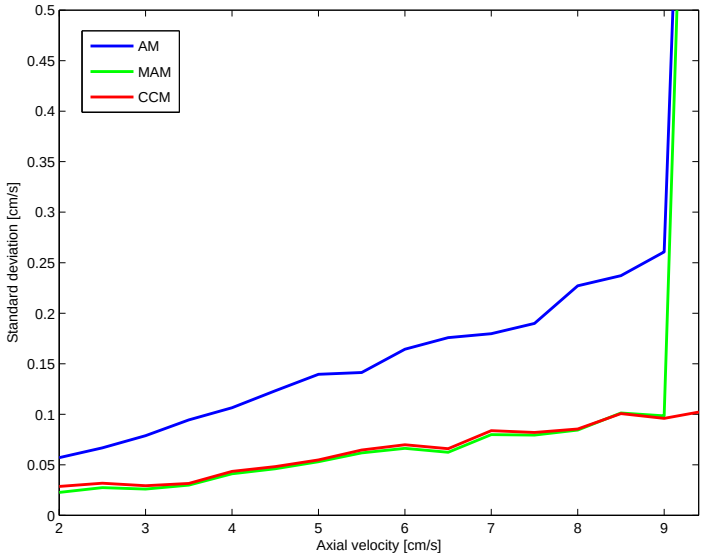

(b) Standard deviation

Figure 4.11: Mean estimated velocity bias and standard deviation as a function of axial velocity using AM, MAM and CCM.

V_{ax} [cm/s]	2	3	4	5	6	7	8
σ_{AM} [cm/s]	0.057	0.079	0.106	0.140	0.164	0.180	0.227
σ_{MAM} [cm/s]	0.023	0.026	0.041	0.053	0.066	0.080	0.084
σ_{CCM} [cm/s]	0.029	0.029	0.044	0.055	0.070	0.084	0.085

Table 4.1: Values for standard deviation from Figure 4.11.

4.4.4 Angle dependency

The intersection angle between the moving scatterers and the ultrasound beam decides the transit time together with beam width and the scatterer's speed. A long transit time gives a narrow-band signal and vice versa. Figure 4.12 shows the velocity estimation bias and standard deviation for the three velocity estimators as a function of intersection angle. Here, the signal from clutter and thermal noise are negligible, and an axial velocity of 8 cm/s is simulated.

4.4.5 Pulse bandwidth

Figure 4.13 shows the velocity estimation bias and standard deviation for the three estimators as a function of $-6dB$ peak pulse bandwidth B_{-6dB}. The signal from moving tissue simulates motion of 8 cm/s towards the transducer, while signal from clutter and thermal noise are negligible.

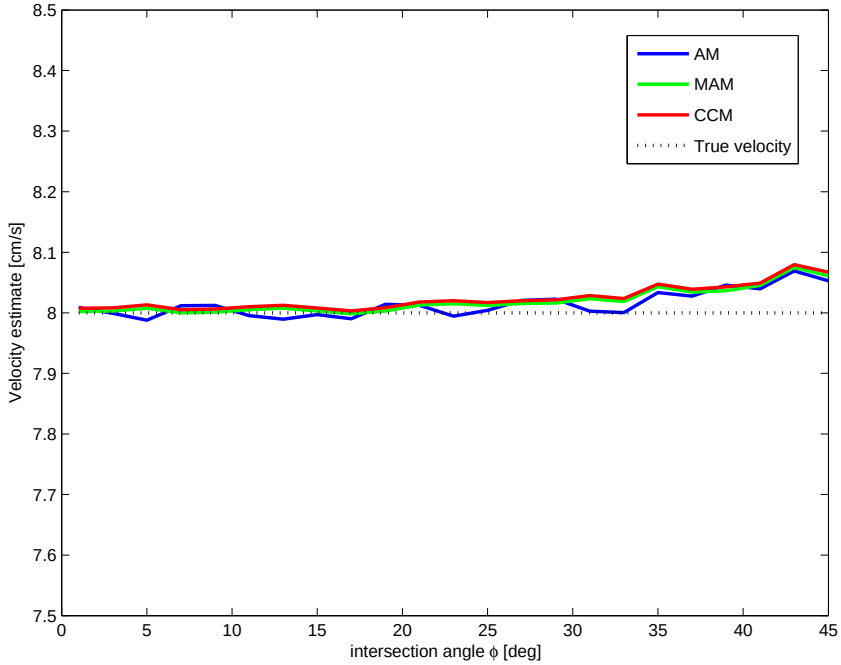

(a) Mean estimates

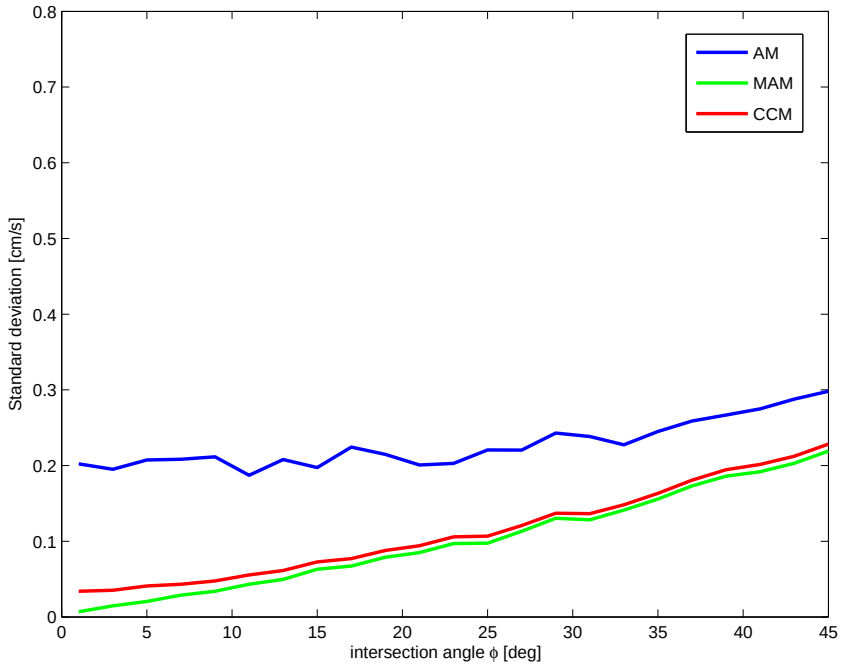

(b) Standard deviation

Figure 4.12: Mean estimated velocity and standard deviation as a function of intersection angle using AM, MAM and CCM.

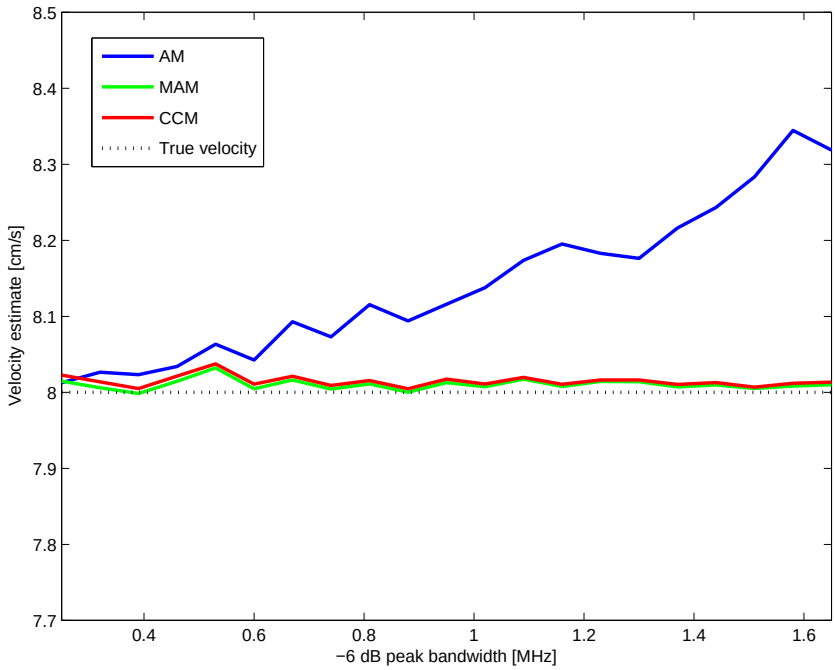

(a) Mean estimates

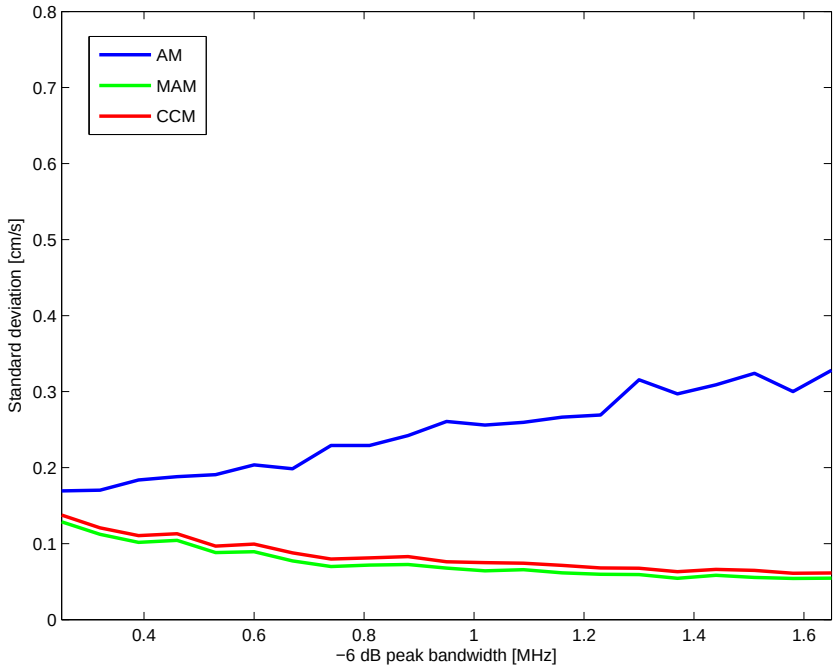

(b) Standard deviation

Figure 4.13: Mean estimated velocity and standard deviation as a function of pulse bandwidth using AM, MAM and CCM.

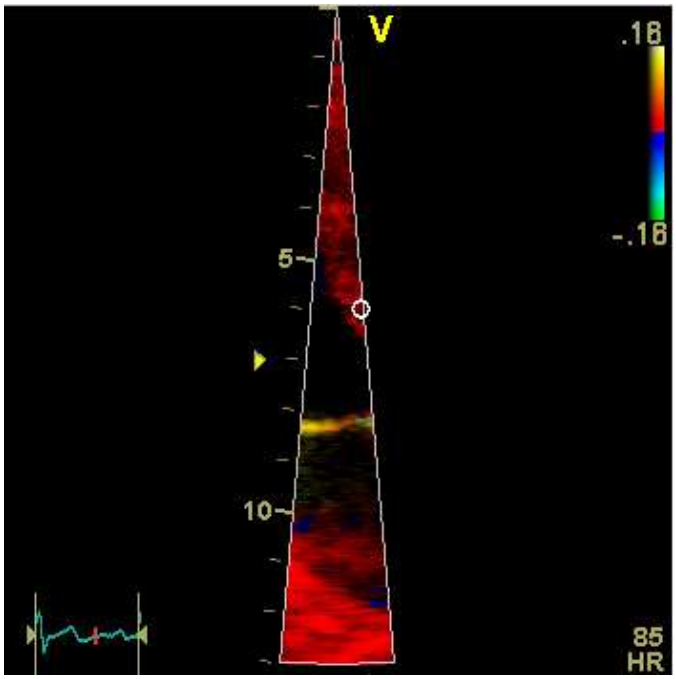

Figure 4.14: One frame of the experimental data applied to velocity estimation. The white circle located in the septum of human heart denotes the mid-point of velocity estimation.

4.5 Velocity estimation on experimental data

Figure 4.14 shows a frame of the narrow acquisition of the septum, located in the upper part of the image, where the white circle denotes the mid-point of the range bin for velocity estimation. The estimated spectral content in terms of radial frequency is shown in Figure 4.15. Next, Figure 4.16 shows the comparison of the velocity curves for the three velocity estimators AM, MAM and CCM, in blue, green and dashed red, respectively. Figure 4.17(a) shows the compensated AM using demodulation frequency equal to 2.31 MHz, the estimated mean radial frequency $\hat{f}_0$ by MAM. The compensation aims to make AM unbiased to ease variance comparison with MAM.

Finally, Figure 4.17(b) shows the velocity difference between AM and MAM, that is, velocity estimated by MAM subtracted from that of AM. The standard deviation of the difference signal $\hat{\sigma}_{\Delta v}$ is estimated to 0.038 cm/s in the interval from $0.18 - 0.32$ seconds.

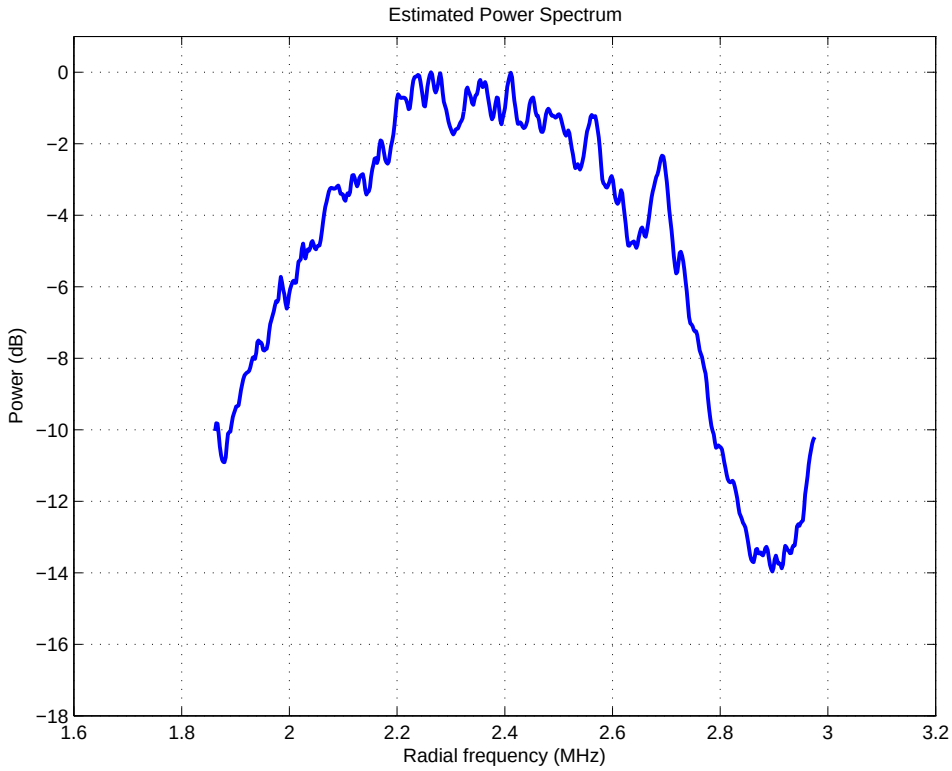

Figure 4.15: Estimated radial frequency content of the full data set shown in Figure 4.14.

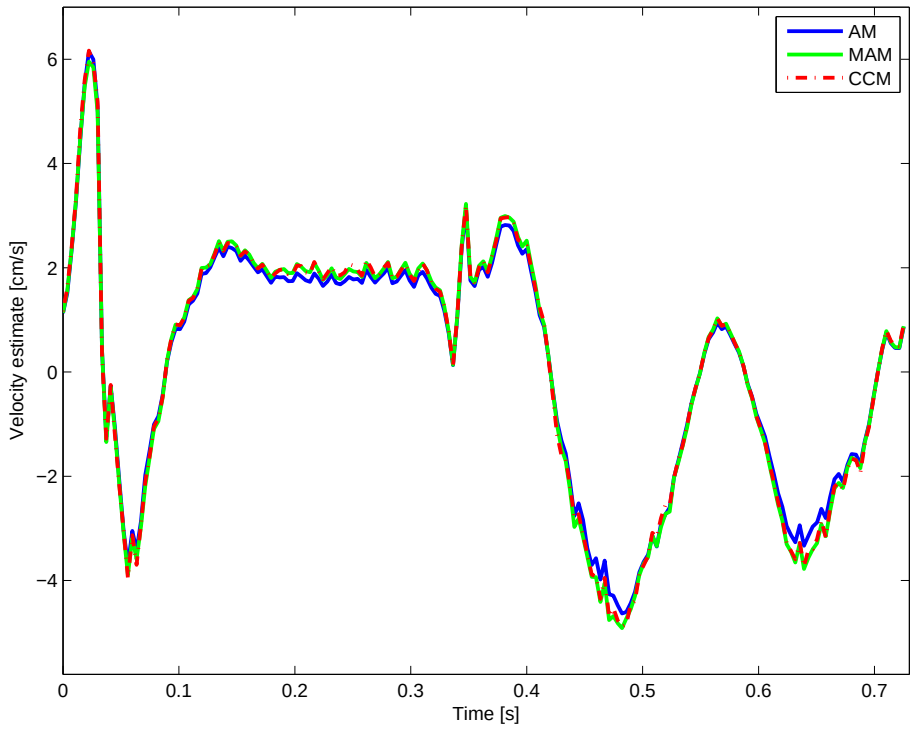

Figure 4.16: Velocity estimation on the experimental data in Figure 4.14. The three velocity estimators AM, MAM and CCM are shown in blue, green and dashed red, respectively.

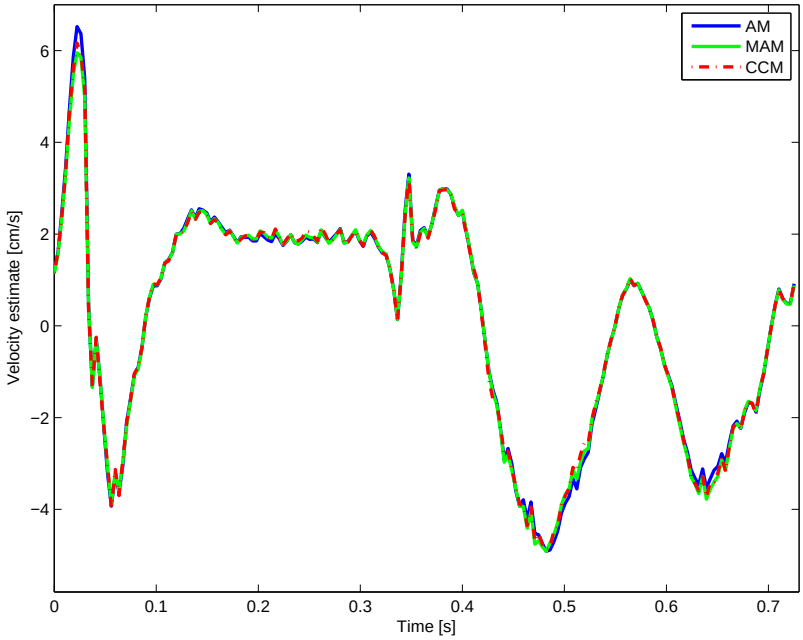

(a) Velocity curves with compensated AM.

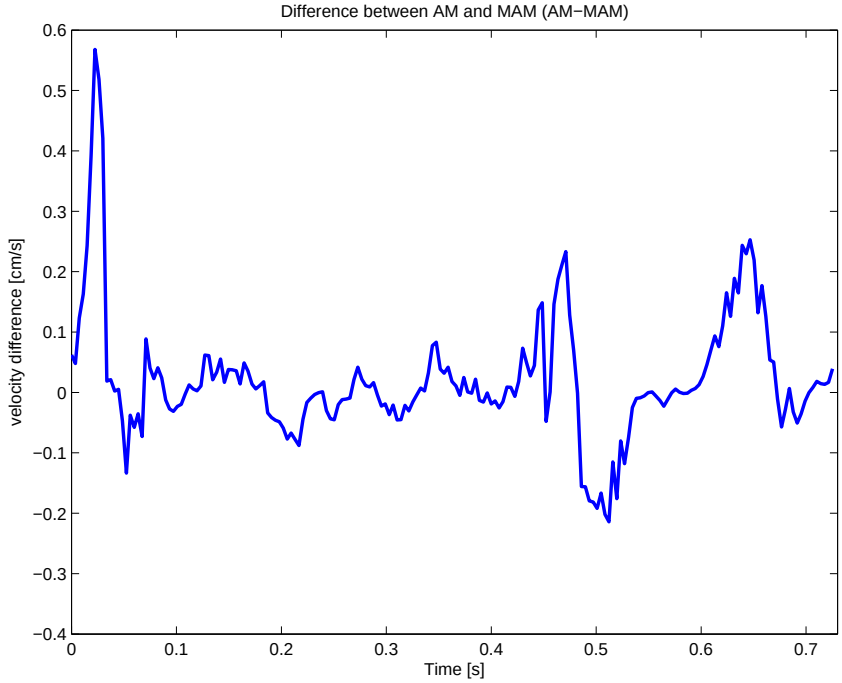

(b) MAM subtracted from AM

Figure 4.17: Velocity curves from Figure 4.16 with compensated AM in upper plot, and estimation difference between AM and MAM in lower plot.

Chapter 5

Discussion

5.1 Simulation model verification

To verify the simulation model developed in this work, the simulated received signal is analysed in frequency and compared to the effective pulse, which represents the intended spectrum. As can be seen in Figure 4.1, the effective pulse spectrum is placed symmetrically within the estimated received signal spectrum. The slightly broader bandwidth of the estimated spectrum is due to smoothing effects caused by the Hamming-window applied to the received signal prior to frequency analysis. In other words, there seems to be good agreement between the intended radial frequency spectrum and that of the received signal.

Further verification comprise qualitative analysis of the received RF-signal in terms of thermal noise, acoustic noise and aliasing. Figure 4.2 demonstrates the disturbance introduced to the RF-signal by thermal noise, where Figure 4.2(a) shows a simulated signal from moving tissue in presence of neither acoustic nor thermal noise. The oblique lines that appear in the RF-signal are a result of the simulated scatterers' movement along the beam, where the slope, compared to a horizontal line, depends on the velocity. Under heavy noise conditions, as in Figure 4.2, the characteristic velocity lines are less evident and nearly vanished. To sum up, the effect of thermal noise added to the velocity signal is clearly confirmed in the RF-domain.

As the clutter signal implemented in this work mimics the artifacts from reverberations, it carries information from simulated sources with low velocities. Figure 4.3 demonstrates the addition of clutter to the signal from moving tissue. Due to the low velocity information, the clutter signal is characterised by some wavy contours along the time scale, where the waviness is proportional to the rms-bandwidth B_{cl} of the Gauss curve the simulation of clutter was based on. This waviness is observed to be more pronounced in Figure 4.3(b) than Figure 4.3(a). That is, the effect of acoustic noise, in terms of clutter, added to the velocity signal has been validated in the

RF-domain.

Aliasing is obtained through decimation of the IQ-data in order to mimic acquisition of velocities higher than the Nyquist velocity, and is exemplified by Figure 4.4. As can be seen, decimation of the unambiguous velocity signal in Figure 4.4(a) results in a signal with ambiguous velocity information as shown in Figure 4.4(b). Here, the originally velocity lines are seen vaguely, while velocity lines with opposite slope sign also appear. Clearly, the effects of aliasing in the velocity signal can be seen in the RF-domain.

In summary, the simulation model developed in this work simulates received echo from moving tissue with acoustic and thermal noise. The tissue movement is limited to constant velocities, the acoustic noise is limited to reverberations, while the thermal noise is similar to general signal loss and receive amplifier noise. The model does not include frequency dependent attenuation. Moreover, the simulated transducer receives data in only one beam, which is sufficient for investigations in this work as exchange of information between beams are not considered. In other words, a simulation environment for evaluation of tissue velocity estimators has successfully been developed.

5.2 Simulation model set-up

The purpose of tuning the simulation model is to approach a realistic environment, given the limitations in the preceding section. First, the spectrum of the simulated received signal is adjusted using an estimated spectrum of a signal acquired with Vivid 7 as reference. As can be seen in Figure 4.5, the mean-square-error approach has lead to reasonable values for both centre frequency and bandwidth for the simulation model. Also the shape of the simulated spectrum is observed to be in pleasing accord with the reference spectrum obtained by Vivid 7.

Second, investigation was carried out to state the repeatability in simulation data applied to tissue velocity estimation. When the number of samples equals 8192, the standard deviation of the estimated standard deviation amounts to 3.1% of the mean estimated standard deviation. This value, which is a measure of the statistical uncertainty in the estimation of standard deviation using the autocorrelation estimator, must be considered sufficiently low to achieve acceptable repeatability. As can be seen in Figure 4.6, simulation with fewer slow-time samples could lead to substantially higher statistical uncertainty.

To sum up, the received echo signal obtained with the simulation model has a spectrum similar to that of signal acquired from a human heart by Vivid 7. Moreover, the uncertainty in standard deviation in tissue velocity estimation amounts to 3.1%, in general, from one set of simulation data to another.

5.3 Clutter filtering

The purpose of clutter filtering is to remove unwanted signal from acoustic sources outside the sample volume to avoid the estimators to take this signal into account when estimating velocities. Figure 4.7 illustrates how the two-dimensional power spectrum is affected by the 1st order FIR filter used for clutter rejection. The filter clearly succeeds in reducing the signal from clutter and low-frequency noise, without affecting the velocity signal to a great extent. As can be seen in Figure 4.8, a negative velocity bias result when the DC-level attenuation of the FIR-filter is decreased. Further it is observed that a positive bias results when the attenuation is increased in an attempt to attain stronger clutter rejection. The positive bias is due to stronger attenuation of the lower frequencies in the velocity signal, leading to a higher mean frequency. Moreover, as low velocity signals are more attenuated than high velocity signals, it is clear that they are more vulnerable to these effects. Since the frequency content of the velocity signal gets more concentrated with higher attenuation the standard deviation decreases as well.

In summary, the clutter signal is evidently reduced by the 1st order FIR filter, which in general increase the mean Doppler frequency of the signal an amount dependent on the signal constitution. Attenuation of 8 dB at DC-level, which is used in this work, introduces a small positive bias for all the estimators, when the simulation of SNR and SCR is 10 dB, while the axial velocity of tissue is 8 cm/s.

5.4 Velocity estimation on simulation data

Data obtained from the simulation model is applied to velocity estimation to investigate to what extent different aspects affect the three velocity estimators. Figure 4.9 illustrates how thermal noise affects estimation of tissue velocities with respect to mean estimates and standard deviation. Presence of thermal noise contributes in principle uniformly to all Doppler frequencies. However, as the clutter filter attenuates the low-frequency noise, the addition of thermal noise results in increased mean Doppler frequency for the signal. As can be seen in Figure 4.9(a), this yields a positive velocity bias that decreases when the SNR increases, and the three estimators are affected to the same extent. Likewise, shown in Figure 4.9(b), increased SNR yields lower standard deviation for all estimators, where CCM and MAM achieve significant lower deviation than AM, provided that the SNR is above 15 dB. However, the three estimators perform similar once the SNR is below 15 dB. That is, dependent on the amount of thermal noise in the simulated signal, the performance of MAM varies from significantly better, to similar performance to that of AM.

Next, investigation of clutter is shown in Figure 4.10. In contrast to thermal noise, clutter presence introduces a negative velocity bias, shown in Figure 4.10(a), since addition of clutter decreases the mean Doppler frequency of the signal. The velocity bias is similar for the three methods, and due to clutter filtering, the bias is insignificant when SCR is above 15 dB. However, the bias increase considerably for SCR below 15 dB. As can be seen in Figure 4.10(b), the standard deviation decreases with increased SCR, and likewise the case with thermal noise, the standard deviation of AM is significantly higher when SCR is above 10 dB. However, the performance of the three estimators approach each other when SCR is below 10. That is, the performance of MAM varies from significantly better, to similar to that of AM, dependent on the amount of clutter present in the simulated signal.

Further, investigation of aliasing is shown in Figure 4.11. As can be seen in Figure 4.11(a), any small bias in AM is proportional with velocity and, thus, more revealing when the velocity is high. MAM and CCM are both unbiased. Now that clutter and thermal noise is negligible, the standard deviation, shown in Figure 4.11(b), is considerably higher for AM than MAM and CCM. This result is in accord with the results above. Interestingly, this difference in standard deviation is increasing with velocity. That is, presence of aliasing in the simulation data harms the performance of AM to a greater extent than MAM and CCM.

Continuing, Figure 4.12 shows the investigation of angle dependency. As can be seen in Figure 4.12(a), increased intersection angle leads to slightly biased estimates. The reduced transit time as a consequence of increased intersection angle, results in velocity signals with broader bandwidth in Doppler frequency. Due to aforementioned effects by clutter filtering the velocity signal, the mean Doppler frequency is slightly increased when the bandwidth is increased. As shown in Figure 4.12(b), the difference in standard deviation between AM and MAM increase in favour of MAM when approaching the optimal intersection angle. Further, the gap is observed to decrease with increasing angle. In other words, the potential in MAM compared to AM, is best exploited when the moving scatterers intersect the ultrasound beam at low angles.

Finally, investigation of pulse bandwidth, found in Figure 4.13, is related to the length of the pulse transmitted by the transducer. The Doppler signal acquired by shorter pulses is broader in frequency due to the broader radial frequency of short pulse lengths. As can be seen in Figure 4.13(a), increased bandwidth results in proportional positive velocity bias for AM, while the mean estimation in MAM and CCM is independent of bandwidth in the range of investigation. This confirms the fact that AM is a narrowband estimator, and shows that MAM and CCM are robust to variation in bandwidth. Moreover, while the standard deviation of AM is observed in Figure 4.13(b) to increase with bandwidth, it decreases slightly for MAM and CCM. That is, using shorter pulses MAM obtain higher radial resolution in

velocity estimates, while the estimation performance is maintained, and even improved. However, because the SNR of the received signal is proportional to bandwidth, the SNR is assumed to increase with bandwidth. Thus, given the noise floor of any system, it is plausible to assume the existence of an optimal working bandwidth for MAM. In this work, the -6 dB peak bandwidth was set equal to 0.7 MHz, which seems to be a fair bandwidth for all estimators.

To sum up, different aspects are investigated using a simulation model that aims at being realistic. Both thermal noise and clutter from reverberations were able to, independently, influence the conditions in disfavour of MAM compared to AM. That is, presence of noise weakens the correlation between radial and Doppler frequency fluctuations, thus, the effect of compensation under such conditions is reduced. A higher SNR can be achieved by increasing the emitted energy. However, there exist limits to the emitted intensities of the ultrasound field [5, Ch. 2.1]. Another approach is to make use of pulse compression, a technique referred to as coded excitation, which intends to increase the SNR without making compromises to spatial resolution. A higher SCR is obtained by increased attenuation of the low frequency components from reverberations. However, increasing the DC-level attenuation of the 1st order FIR filter used in this work, leads to significant estimation bias. Another approach is to use higher order filters that can achieve stronger attenuation in stop band, and shorter transition interval between stop and pass band. Using multi-line acquisition (MLA) to obtain high frame rate with packet size 1, higher order clutter filters can be applied to a corresponding number of slow-time samples. In contrast to thermal noise and clutter, the presence of aliasing did not show capabilities to disfavour MAM, but on the other hand shown to harm AM more than MAM. Finally, there are more potential in the performance of MAM when it comes to both angle dependency and bandwidth, but the values used in this work has shown to be fair to all estimators.

5.5 Velocity estimation on experimental data

The estimation of the mean received radial frequency by MAM to be 2.31 MHz is in good accord with the estimated spectre in Figure 4.15. As can be observed by comparing the velocity curves in Figure 4.16 and Figure 4.17(a), the bias effect in AM is to be reduced when compensated demodulation frequency is used. The variance could not be qualitatively approved lower for MAM than AM, like it was when the estimators were applied to blood velocity estimation in [7].

In general, Figure 4.17(b) shows largest deviation between AM and MAM at points with peak velocities, which corresponds well with results from Figure 4.11. The difference signal presents the variation in deviation between

the two estimators, and give no direct information about performance on either of them, only on the relation between them. Nevertheless, the standard deviation of the difference signal $\sigma_{\Delta v}$ is dependent on the correlation in error estimation done by the two estimators, where a high correlation would reduce the deviation. On the other hand, the deviation will increase when the estimation error between the two estimators is uncorrelated. The standard deviation of the difference signal $\hat{\sigma}_{\Delta v}$ is estimated to be 0.038 cm/s in the interval from $0.18 - 0.32$ seconds, where the axial velocity is approximately 2 cm/s. Using results from simulations with similar set-up parameters and axial velocity, the expected standard deviation can be calculated. From Table 4.1, the standard deviations for AM σ_{AM} and MAM σ_{MAM} in a noise-free environment is found to be 0.057 and 0.023, when the axial velocity is 2 cm/s. Assuming uncorrelated estimation error between AM and MAM, the expected standard deviation of the difference $\sigma_{\Delta v}$ is given by $\sigma_{\Delta v} = \sqrt{\sigma_{AM}^2 + \sigma_{MAM}^2} = 0.062$. This result claims that the estimation error in AM and MAM is correlated for the experimental data, as the estimated standard deviation of the difference signal $\hat{\sigma}_{\Delta v}$ is significantly lower than expected for a noise-free environment. That is, at least one source to error is likely to introduce correlation between the estimation error in AM and MAM.

However, one should be careful to rule out other unknown factors that corrupt velocity estimation. As an example, Figure 4.15 reveals probable aliasing in the fast-time signal, a factor not considered up to this point. Such aliasing cause low-frequency content to be misplaced in the upper part of the spectre. Although it is difficult, without further investigation, to suggest how the present aliasing affected velocity estimation in this work, it is plausible to assume MAM more vulnerable to fast-time aliasing than AM. This because the continuously frequency compensation in MAM is based on direct estimation in the radial frequency domain, while AM estimates are fully based on the slow-time signal.

In summary, estimation of radial centre frequency reduced the bias effect in AM when replacing the demodulation frequency. In fact, while AM is vulnerable to frequency dependent attenuation, MAM remains unbiased by means of frequency compensation. On the other hand, a lower estimation variance could qualitatively not be approved with continuously frequency compensation. Furthermore, statistical analysis based on expected values from simulations demonstrated correlation between the estimation error in AM and MAM.

Chapter 6

Conclusion

Strain Rate Imaging was introduced as a clinical tool to quantify regional myocardial deformation. As the method is velocity-based and very sensitive to noise, precise velocity estimates are essential to achieve acceptable performance. An extended version of the widely used autocorrelation estimator (AM), exploit correlation in radial and Doppler frequency fluctuations to obtain lower estimation variance. The approach, referred to as the modified autocorrelation method (MAM), has previously shown superior performance in low-noise simulation environments, but lacks to show equivalent results when applied to in-vivo experiments.

A simulation model for evaluation of tissue velocity estimators was successfully developed. The model includes realistic aspects like thermal noise, typical acoustic noise from reverberations, and aliasing. Parameters and data from experimental acquisition was used as a reference in order to achieve realistic simulated acquisition settings like centre frequency, bandwidth and beam width. When a 1st order FIR filter was used for clutter rejection, investigations shown that thermal noise and clutter signal from reverberations, independently, were able to disfavour MAM to a greater extent than AM. The performance of MAM went from significantly better in low-noise conditions, to approaching AM when SNR and SCR became lower than 15 and 10 dB, respectively. The presence of any noise weakens the correlations in radial and Doppler frequency fluctuations, and thus reduce the compensation effect.

Velocity estimation on experimental data shown MAM's robustness to frequency dependent attenuation. MAM remains unbiased by means of frequency compensation, while AM suffers from bias effects. However, continuously frequency compensation failed to approve lower estimation variance for MAM compared to AM. Finally, by means of statistical analysis, correlation between estimation error in AM and MAM was demonstrated when applied to experimental data.

Future work

Future work may comprise:

- further investigation, in a simulated environment, of the correlation between estimation error made by AM and MAM.
- investigation of the use of higher order clutter filters prior to tissue velocity estimation. This can be realised through the use of MLA to obtain high frame rate in continuous acquisition (packet size 1).
- investigation of the performance of MAM with respect to the relation between pulse bandwidth and the system noise floor. It is plausible to assume an optimal working bandwidth for MAM given a noise floor level.
- Finally, effort should be put into development of a model to simulate tissue velocities that vary with time and space. This would allow for simulation of strain rate.

Bibliography

[1] Bjørn A.J. Angelsen. Waves, signals and signal processing in medical ultrasonics, volume 1, 1996.

[2] Bjørn A.J. Angelsen. Waves, signals and signal processing in medical ultrasonics, volume 2, 1996.

[3] Ann E.A. Blomberg, Andreas Heimdal, Stein Inge Rabben, Jan D'hooge, and Andreas Austeng. Evaluation of a modified autocorrelation method when applied to cardiac strain rate imaging, 2005.

[4] A. Heimdal, A. Støylen, H. Torp, and T. Skjærpe. Real-time strain rate imaging of the left ventricle by ultrasound. *Journal of the American Society of Echocardiography*, (11):1013–1019, 1998.

[5] Jørgen Arendt Jensen. *Estimation of Blood Velocities Using Ultrasound*. Cambridge University Press, 1996.

[6] C. Kasai and K. Namekawa. Real-time two dimensional blood flow imaging using an autocorrelation technique. *IEEE Utrasonics symposium*, pages 953–958, 1985.

[7] Xiaoming Lai, Hans Torp, and Kjell Kristoffersen. An extended autocorrelation method for estimation of blood velocity. *IEEE Transactions on Ultrasonics, Ferroelectrics, and Frequency Control*, 44(6), 1997.

[8] Lasse Løvstakken. *Signal processing in diagnostic ultrasound: Algorithms for real-time estimation and visualization of blood flow velocity*. PhD thesis, Norwegian University of Science and Technology, 2007.

[9] W.M. McDicken, G.R. Sutherland, C.M. Moran, and L.N. Gordon. Colour doppler velocity imaging of the myocardium. *Ultrasound in Medicine and Biology*, (18):651–654, 1992.

[10] John G. Proakis and Dimitris G. Manolakis. *Digital signal processing*. Prentice Hall International, third edition, 1996.

[11] G.R. Sutherland, L. Hatle, P. Claus, J. D'hooge, and B.H. Bijnens. Doppler myocardial imaging, 2006.

[12] J.T. Powers Thanasis Loupas and Robert W. Gill. An axial velocity estimator for ultrasound blood flow imaging, based on a full evaluation of the doppler equation by means of a two dimensional autocorrelation approach. *IEEE Transactions on Ultrasonics, Ferroelectrics, and Frequency Control*, 42(4):672–688, 1995.

[13] Hans Torp. Clutter rejection filters in color flow imaging: A theoretical approach. *IEEE Transactions on ultrasonics, ferroelectrics, and frequency control*, 1997.